WILEY

Material nonlinear topology optimization considering the von Mises criterion through an asymptotic approach: Max strain energy and max load factor formulations

Tuo Zhao[1] | Adeildo S. Ramos Jr.[2] | Glaucio H. Paulino[1]

[1]School of Civil and Environmental Engineering, Georgia Institute of Technology, Atlanta, Georgia

[2]Center of Technology, Federal University of Alagoas, Maceió, Brazil

Correspondence
Glaucio H. Paulino, School of Civil and Environmental Engineering, Georgia Institute of Technology, 790 Atlantic Drive, Atlanta, GA 30332.
E-mail: paulino@gatech.edu

Summary

This paper addresses material nonlinear topology optimization considering the von Mises criterion by means of an asymptotic analysis using a fictitious nonlinear elastic model. In this context, we consider the topology optimization problem subjected to prescribed energy, which leads to robust convergence in nonlinear problems. Two nested formulations are considered. In the first, the objective is to maximize the strain energy of the system in equilibrium, and in the second, the objective is to maximize the load factor. In both cases, a volume constraint is imposed. The sensitivity analysis is quite effective and efficient in the sense that there is no extra adjoint equation. In addition, the nonlinear structural equilibrium problem is solved using direct minimization of the structural strain energy using Newton's method with an inexact line-search strategy. Four numerical examples demonstrate the features of the proposed material nonlinear topology optimization framework for approximating standard von Mises plasticity.

KEYWORDS

asymptotic analysis, material nonlinearity, nonlinear elastic constitutive model, topology optimization, von Mises criterion

1 | INTRODUCTION

Topology optimization has been widely used in different industrial/academic problems in the last few decades. Despite its level of maturity, most previous studies focused on linear materials and omitted the nonlinearity of real-life materials. Plastic material models addressed in topology optimization problems include the works of Yuge and Kikuchi,[1] Swan and Kosaka,[2] Maute et al,[3] Schwarz et al,[4] Yoon and Kim,[5] Bogomolny and Amir,[6] James and Waisman,[7] Kato et al,[8] Nakshatrala and Tortorelli,[9] Wallin et al,[10] Xia et al,[11] and Alberdi and Khandelwal,[12] which is just a small sample of references in the field. Due to material path dependence, the sensitivity will also be path dependent. In this paper, we propose a topology optimization approach that indirectly takes into account plastic material behavior by means of a

Nomenclature: τ_y, shear yield stress; σ_y, uniaxial yield stress; $\boldsymbol{\sigma}$, stress tensor; $\boldsymbol{\sigma}_d$, deviatoric stress tensor; K, material bulk modulus; μ, material shear modulus; $\boldsymbol{\varepsilon}$, strain tensor; $\boldsymbol{\varepsilon}_d$, deviatoric strain tensor; ε_v, volumetric strain; ε_{ref}, small reference strain; φ, strain energy density; φ_e, specific strain energy density function of element e; U, strain energy; C_0, prescribed energy; $\boldsymbol{f}_0$, vector of given applied forces; $\boldsymbol{u}$, nodal displacement vector; ρ, vector of element density variables; $\overline{\rho}$, elements' physical densities; r_{min}, filter radius; q, order of filter; p, constant penalty; n, number of elements discretizing the design domain; v_e, volume of element e; V_{max}, maximum material volume; $\boldsymbol{T}$, internal force vector; λ, reaction load factor; $\boldsymbol{K}_T$, tangent stiffness matrix; $\boldsymbol{D}$, consistent tangent matrix; $\Delta\boldsymbol{u}$, Newton step; α, step size by backtracking line search; J, objective function; $\mathcal{L}$, Lagrangian function; p_{lim}, limit pressure; w, magnitude of distributed load; β, Tikhonov regularization parameter.

fictitious nonlinear elastic constitutive model, shown as the red curve in Figure 1. Pasquali[13] used this nonlinear elastic model for simulating the elastic-plastic behavior of structures through limit analysis. His nonlinear elastic constitutive model is inspired by the deformation theory of plasticity.[14] The numerical tests show that, at the limit state, the nonlinear elastic solution is equivalent to the plastic solution.

This study proposes two nested formulations. In the first formulation, the objective function of the optimization problem consists of maximizing the strain energy of the system in equilibrium. In the second formulation, the objective function consists of maximizing the load factor of the system in equilibrium. Both formulations limit the total volume of the structure and lead to optimal designs in terms of stiffness. The sensitivity analysis using the proposed nonlinear elastic model does not require an extra adjoint equation.

In order to solve the nonlinear state equations, we use an energy control approach, which is illustrated in Figure 2. This approach prescribes a certain value of energy, C_0, for all design cycles until the optimal design is obtained. Choosing an appropriate value of C_0 is possible if the designer has some knowledge regarding the expected nonlinear material behavior. Alternatively, the designer can select C_0 to ensure that the material reaches the von Mises limit stage. For plastic material models, the energy control approach has better convergence behavior than the load control method. Crisfield[15] pointed out that load control is not preferable when a small addition to the load causes a relatively large additional displacement or when limit points are encountered. The energy control approach overcomes this difficulty in regions where the stress state tends to go beyond the yielding limit. The numerical results show that the energy control approach leads to robust convergence in solving nonlinear state equations.

This paper first discusses the nonlinear constitutive model in Section 2. The optimization formulations and the related sensitivity analysis are presented in Section 3. Section 4 discusses the finite element method (FEM) in terms of solving nonlinear state equations. The energy control approach is discussed in detail in this section. Section 5 discusses a verification of the present FEM approach. Four numerical examples are illustrated in Section 6—it includes an investigation of the structural performance for three optimized structures considering either classical Mises plasticity or the nonlinear elastic model. Conclusions are presented in Section 7. Finally, six appendices complement the manuscript. In particular, Appendix A presents the plane strain nonlinear elastic constitutive model; Appendix B states the lower-bound
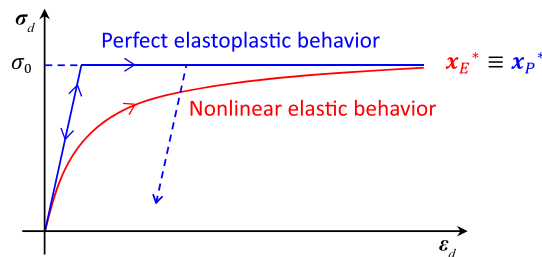

FIGURE 1 Illustration of the nonlinear elastic material constitutive model compared with the von Mises perfect elastoplastic model. Notice that in the limit, both models converge to $x_E^* = x_P^*$
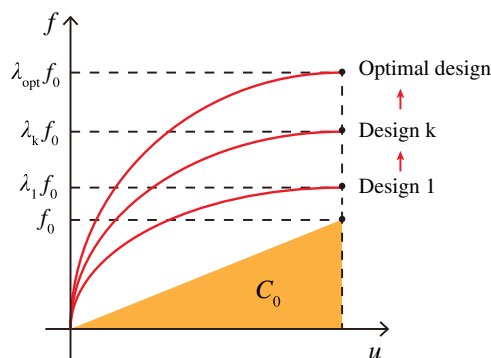

FIGURE 2 Illustration of the proposed energy control approach. The approach prescribes a certain value of energy C_0 for all design cycles until the optimal design is obtained. In this illustration, we assume that the load factor at the kth design cycle $\lambda_k > 1$ and the load reference f_0 is a single applied load. For further details, see Appendices E and F [Colour figure can be viewed at wileyonlinelibrary.com]

theorem; Appendix C presents the failure mechanism of the optimized clamped beam structure from one of the examples in the paper; Appendix D addresses the filter continuation scheme; and finally, Appendices E and F present the choice of the prescribed energy parameter C_0 and a related one-bar truss example, respectively.

2 | EQUIVALENT NONLINEAR ELASTIC CONSTITUTIVE MODEL

We consider nonlinear material behavior by means of an asymptotic analysis using a fictitious nonlinear elastic model. The material nonlinear elastic model is governed by the von Mises criterion.[16] The yield function is defined as

$$f(\boldsymbol{\sigma}) = \|\boldsymbol{\sigma}_d\| - \sqrt{2}\,\tau_y \le 0, \tag{1}$$

where τ_y is the shear yield stress, the tensor $\boldsymbol{\sigma}_d$ is the deviatoric component of the stress tensor $\boldsymbol{\sigma}$, and the norm of $\boldsymbol{\sigma}_d$ is written as $\|\boldsymbol{\sigma}_d\| = \sqrt{\boldsymbol{\sigma}_d : \boldsymbol{\sigma}_d}$.

We use the nonlinear elastic constitutive relationship[13] in the following form:

$$\boldsymbol{\sigma} = K\varepsilon_v \boldsymbol{I} + 2\mu\left(\|\boldsymbol{\varepsilon}_d\|\right)\boldsymbol{\varepsilon}_d, \tag{2}$$

where the constant K is the material bulk modulus and the scalar $\varepsilon_v = \text{tr}(\boldsymbol{\varepsilon})$ is the volumetric strain. The tensor $\boldsymbol{\varepsilon}_d$ is the deviatoric component of the strain tensor $\boldsymbol{\varepsilon}$, and the norm of $\boldsymbol{\varepsilon}_d$ is written as $\|\boldsymbol{\varepsilon}_d\| = \sqrt{\boldsymbol{\varepsilon}_d : \boldsymbol{\varepsilon}_d}$. The shear modulus $\mu(\|\boldsymbol{\varepsilon}_d\|)$ is a function of $\|\boldsymbol{\varepsilon}_d\|$.

The nonlinear constitutive relation is defined such that the stress $\boldsymbol{\sigma}$ defined in Equation (2) asymptotically satisfies Equation (1). For relatively large values of $\|\boldsymbol{\varepsilon}_d\|$, condition (1) is considered to be active, ie,

$$\lim_{(\varepsilon_d/\varepsilon_{\text{ref}}) \to \infty} f\left(K\varepsilon_v \boldsymbol{I} + 2\mu\left(\|\boldsymbol{\varepsilon}_d\|\right)\boldsymbol{\varepsilon}_d\right) = 0, \tag{3}$$

where the reference strain ε_{ref} is a small value that is a fraction of the strain that at the end of the elastic region. Equation (3) implies that the shear modulus $\mu(\|\boldsymbol{\varepsilon}_d\|)$ satisfies

$$\mu\left(\|\boldsymbol{\varepsilon}_d\|\right) \approx \frac{\sqrt{2}\tau_y}{2\,\|\boldsymbol{\varepsilon}_d\|} \quad \text{if} \quad \frac{\|\boldsymbol{\varepsilon}_d\|}{\varepsilon_{\text{ref}}} \gg 1. \tag{4}$$

We adopt the following form of $\mu(\|\boldsymbol{\varepsilon}_d\|)$ to simulate the asymptotic behavior of the nonlinear elastic constitutive model in Equation (2):

$$\mu\left(\|\boldsymbol{\varepsilon}_d\|\right) = \frac{\sqrt{2}\tau_y}{2}\frac{1}{\varepsilon_{\text{ref}} + \|\boldsymbol{\varepsilon}_d\|}. \tag{5}$$

Figure 3 illustrates the nonlinear elastic model in Equation (2) with different choices of ε_{ref}. Notice that as ε_{ref} decreases, a rigid plastic behavior is approached. From Equation (5), we note that shear modulus μ tends to zero for relatively large
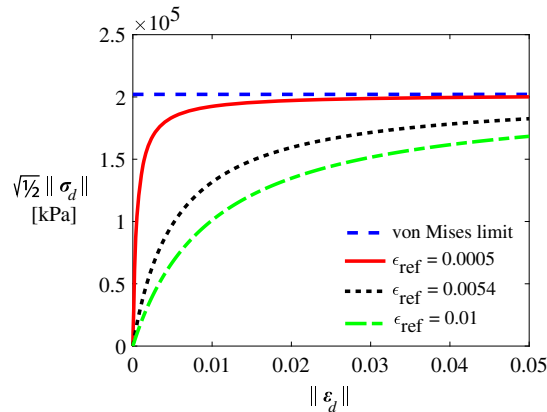

FIGURE 3 Behavior of the proposed nonlinear elastic constitutive model with different choices of reference strain ε_{ref}. The material properties considered are the following: $E = 71 \times 10^6$ kPa, $\tau_y = 2.02 \times 10^5$ kPa, and $\upsilon = 0.33$ [Colour figure can be viewed at wileyonlinelibrary.com]

$\|\varepsilon_d\|$. The bulk modulus K remains constant. Thus, we have

$$\lim_{(\varepsilon_d/\varepsilon_{\text{ref}})\to\infty} \frac{\mu(\|\varepsilon_d\|)}{K} = 0, \tag{6}$$

which implies that the nonlinear elastic model behaves as an incompressible material in the asymptotic region (ie, yield region).

The nonlinear elastic constitutive model in Equation (2) can be characterized by the strain energy density $\varphi(\varepsilon_v, \|\varepsilon_d\|)$ such that the stress tensor is given by

$$\boldsymbol{\sigma} = \frac{\partial \varphi(\varepsilon_v, \|\varepsilon_d\|)}{\partial \boldsymbol{\varepsilon}} = \frac{\partial \varphi}{\partial \varepsilon_v}\frac{\partial \varepsilon_v}{\partial \boldsymbol{\varepsilon}} + \frac{\partial \varphi}{\partial \|\varepsilon_d\|}\frac{\partial \|\varepsilon_d\|}{\partial \boldsymbol{\varepsilon}} = \frac{\partial \varphi}{\partial \varepsilon_v}\boldsymbol{I} + \frac{\partial \varphi}{\partial \|\varepsilon_d\|}\frac{1}{\|\varepsilon_d\|}\boldsymbol{\varepsilon}_d. \tag{7}$$

From Equations (2) and (7), we obtain

$$\frac{\partial \varphi(\varepsilon_v, \|\varepsilon_d\|)}{\partial \varepsilon_v} = K\varepsilon_v \text{ and } \frac{\partial \varphi(\varepsilon_v, \|\varepsilon_d\|)}{\partial \|\varepsilon_d\|} = 2\mu(\|\varepsilon_d\|)\|\varepsilon_d\|. \tag{8}$$

By solving the differential equation in (7), we obtain the explicit expression of $\varphi(\varepsilon_v, \|\varepsilon_d\|)$ as

$$\varphi(\varepsilon_v, \|\varepsilon_d\|) = \frac{1}{2}K\varepsilon_v^2 + \sqrt{2}\tau_y\left(\ln\left(\left(\frac{\varepsilon_{\text{ref}}}{\|\varepsilon_d\|+\varepsilon_{\text{ref}}}\right)^{\varepsilon_{\text{ref}}}\right) + \|\varepsilon_d\|\right). \tag{9}$$

3 | OPTIMIZATION FORMULATIONS AND SENSITIVITY ANALYSES

We propose two nested formulations[17] with different objectives. In the first formulation, the objective function of the optimization problem consists of maximizing the strain energy of the system in equilibrium subjected to a volume constraint. In the second formulation, the objective function of the optimization problem consists of maximizing the reaction load factor of the system in equilibrium subjected to a volume constraint. In both formulations, we consider the nonlinear state problem subjected to prescribed energy.

3.1 | Nested formulation: maximizing structural strain energy

We consider the following nested formulation for the optimization problem of maximizing structural strain energy with prescribed energy in the state equations:

$$\begin{aligned} \max_{\boldsymbol{\rho}} \quad & J_U(\boldsymbol{\rho}) := U(\boldsymbol{\rho}, \boldsymbol{u}(\boldsymbol{\rho})) \\ \text{s.t.} \quad & \begin{cases} \sum_{e=1}^n \rho_e v_e \le V_{\max} \\ 0 < \rho_{\min} \le \rho_e \le 1 \end{cases} \\ \text{with} \quad & \begin{cases} \boldsymbol{T}(\boldsymbol{\rho}, \boldsymbol{u}(\boldsymbol{\rho})) = \lambda(\boldsymbol{\rho}, \boldsymbol{u}(\boldsymbol{\rho}))\boldsymbol{f}_0 \\ \boldsymbol{f}_0^{\mathrm{T}}\boldsymbol{u}(\boldsymbol{\rho}) = 2C_0. \end{cases} \end{aligned} \tag{10}$$

The objective function $U(\boldsymbol{\rho}, \boldsymbol{u}(\boldsymbol{\rho}))$ is the structural strain energy. The design variable $\boldsymbol{\rho}$ is a vector of element material densities. The parameter n represents the number of elements used to discretize the design domain, v_e is the volume of element e, $V_{\max}$ is the maximum material volume, and $\rho_{\min}$ denotes the lower bound of the design variable, which is introduced to prevent numerical singularity in the design domain.[18] Here, $\boldsymbol{T}(\boldsymbol{\rho}, \boldsymbol{u}(\boldsymbol{\rho}))$ is the internal force vector, $\lambda(\boldsymbol{\rho}, \boldsymbol{u}(\boldsymbol{\rho}))$ is the load factor, $\boldsymbol{f}_0$ is the vector of given external forces, and C_0 is the prescribed energy in the structural system.

For structures subjected to prescribed energy and given fixed supports, maximizing the structural strain energy is equivalent to maximizing structural stiffness,[19,20] ie, in the case of linear elasticity, the results obtained using the proposed formulation will be identical to those of the minimum compliance problem. This aspect is illustrated through a simple example in Appendix F.

3.2 | Sensitivity analysis for max strain energy

We derive the sensitivities of the objective function and constraints for the optimization problem of Equation (10). We can easily obtain the sensitivity of the constraints that are linear with respect to design variables ρ. Differentiating the objective function and using the chain rule, we obtain the following equality:

$$\frac{dJ_U(\rho)}{d\rho_e} = \frac{\partial U(\rho, \boldsymbol{u}(\rho))}{\partial \rho_e} + \left[\frac{\partial U(\rho, \boldsymbol{u}(\rho))}{\partial \boldsymbol{u}(\rho)}\right]^{\mathrm{T}} \frac{\partial \boldsymbol{u}(\rho)}{\partial \rho_e} = \frac{\partial U(\rho, \boldsymbol{u}(\rho))}{\partial \rho_e} + [\boldsymbol{T}(\rho, \boldsymbol{u}(\rho))]^{\mathrm{T}} \frac{\partial \boldsymbol{u}(\rho)}{\partial \rho_e}. \tag{11}$$

In (11), the term $\partial U(\rho, \boldsymbol{u}(\rho))/\partial \rho_e$ can be evaluated explicitly. In order to evaluate the remaining term, we substitute one of the state equations $\boldsymbol{T}(\rho, \boldsymbol{u}(\rho)) = \lambda(\rho, \boldsymbol{u}(\rho))\boldsymbol{f}_0$ into (11) to obtain the expression

$$\frac{dJ_U(\rho)}{d\rho_e} = \frac{\partial U(\rho, \boldsymbol{u}(\rho))}{\partial \rho_e} + \lambda(\rho, \boldsymbol{u}(\rho))\, \boldsymbol{f}_0^{\mathrm{T}}\, \frac{\partial \boldsymbol{u}(\rho)}{\partial \rho_e}. \tag{12}$$

In order to evaluate $\partial \boldsymbol{u}(\rho)/\partial \rho_e$ in (11), we differentiate the other state equation $\boldsymbol{f}_0^{\mathrm{T}}\boldsymbol{u}(\rho) = 2C_0$ with respect to ρ_e, ie,

$$\boldsymbol{f}_0^{\mathrm{T}}\frac{\partial \boldsymbol{u}(\rho)}{\partial \rho_e} = \frac{\partial 2C_0}{\partial \rho_e} = 0. \tag{13}$$

By substituting (13) into (12), we obtain the final expression of the sensitivity of the objective function as follows:

$$\frac{dJ_U(\rho)}{d\rho_e} = \frac{\partial U(\rho, \boldsymbol{u}(\rho))}{\partial \rho_e}, \tag{14}$$

which is elegant in the sense that there is no need for introducing an extra adjoint problem since the formulation of maximizing structural strain energy is self-adjoint. Compared to other formulations (see, for example, the work of Alberdi and Khandelwal[12]), the sensitivity analysis is simple and efficient.

3.3 | Alternative nested formulation: maximizing load factor

We consider the following nested formulation for the optimization problem of maximizing the load factor with prescribed energy in the system:

$$\max_{\rho} \; J_\lambda(\rho) := \lambda(\rho, \boldsymbol{u}(\rho))$$

$$\text{s.t.} \begin{cases} \displaystyle\sum_{e=1}^{n} \rho_e v_e \leq V_{\max} \\ 0 < \rho_{\min} \leq \rho_e \leq 1 \end{cases} \tag{15}$$

$$\text{with}$$

$$\begin{cases} \boldsymbol{T}(\rho, \boldsymbol{u}(\rho)) = \lambda(\rho, \boldsymbol{u}(\rho))\boldsymbol{f}_0 \\ \boldsymbol{f}_0^{\mathrm{T}}\boldsymbol{u}(\rho) = 2C_0. \end{cases}$$

3.4 | Sensitivity analysis for max load factor

We derive the sensitivities of the objective function and constraints for the optimization problem of Equation (15). We can easily obtain the sensitivity of the constraints that are linear with respect to design variables ρ. In order to evaluate the sensitivity of the objective function $\lambda(\rho, \boldsymbol{u}(\rho))$, we differentiate one of the state equations $\boldsymbol{T}(\rho, \boldsymbol{u}(\rho)) = \lambda(\rho, \boldsymbol{u}(\rho))\boldsymbol{f}_0$ with respect to ρ_e, ie,

$$\frac{\partial \boldsymbol{T}(\rho, \boldsymbol{u}(\rho))}{\partial \rho_e} + \left[\frac{\partial \boldsymbol{T}(\rho, \boldsymbol{u}(\rho))}{\partial \boldsymbol{u}}\right]^{\mathrm{T}} \frac{\partial \boldsymbol{u}(\rho)}{\partial \rho_e} = \frac{d\lambda(\rho, \boldsymbol{u}(\rho))}{d\rho_e}\boldsymbol{f}_0, \tag{16}$$

where $\partial \boldsymbol{T}(\rho, \boldsymbol{u}(\rho))/\partial \boldsymbol{u}(\rho) = \boldsymbol{K}_T(\rho, \boldsymbol{u}(\rho))$, which is the tangent stiffness matrix. From (16), we compute

$$\frac{\partial \boldsymbol{u}(\rho)}{\partial \rho_e} = [\boldsymbol{K}_T(\rho, \boldsymbol{u}(\rho))]^{-\mathrm{T}}\frac{d\lambda(\rho, \boldsymbol{u}(\rho))}{d\rho_e}\boldsymbol{f}_0 - [\boldsymbol{K}_T(\rho, \boldsymbol{u}(\rho))]^{-\mathrm{T}}\frac{\partial \boldsymbol{T}(\rho, \boldsymbol{u}(\rho))}{\partial \rho_e}. \tag{17}$$

By multiplying $\boldsymbol{f}_0^{\mathrm{T}}$ on both sides of Equation (17), we arrive at

$$\boldsymbol{f}_0^{\mathrm{T}}\frac{\partial \boldsymbol{u}}{\partial \rho_e} = \boldsymbol{f}_0^{\mathrm{T}}(\boldsymbol{K}_T)^{-\mathrm{T}}\frac{d\lambda}{d\rho_e}\boldsymbol{f}_0 - \boldsymbol{f}_0^{\mathrm{T}}(\boldsymbol{K}_T)^{-\mathrm{T}}\frac{\partial \boldsymbol{T}}{\partial \rho_e}. \tag{18}$$

According to Equation (13), $\boldsymbol{f}_0^{\mathrm{T}} (\partial \boldsymbol{u}/\partial \rho_e) = 0$, and thus, we obtain

$$\frac{d\lambda}{d\rho_e} = \frac{\boldsymbol{f}_0^{\mathrm{T}}(\boldsymbol{K}_T)^{-\mathrm{T}}\frac{\partial \boldsymbol{T}}{\partial \rho_e}}{\boldsymbol{f}_0^{\mathrm{T}}(\boldsymbol{K}_T)^{-\mathrm{T}}\boldsymbol{f}_0} = \frac{\left(\frac{\partial \boldsymbol{T}}{\partial \rho_e}\right)^{\mathrm{T}}(\boldsymbol{K}_T)^{-\mathrm{T}}\boldsymbol{f}_0}{\boldsymbol{f}_0^{\mathrm{T}}(\boldsymbol{K}_T)^{-\mathrm{T}}\boldsymbol{f}_0} = \frac{\left(\frac{\partial \boldsymbol{T}}{\partial \rho_e}\right)^{\mathrm{T}}\boldsymbol{u}_0}{\boldsymbol{f}_0^{\mathrm{T}}\boldsymbol{u}_0}, \tag{19}$$

where $\boldsymbol{u}_0 = (\boldsymbol{K}_T)^{-\mathrm{T}}\boldsymbol{f}_0$. Since there is no need for the adjoint problem, the sensitivity analysis is again simple, effective, and efficient.

4 | SOLVING THE NONLINEAR STATE EQUATIONS: NEWTON'S METHOD WITH LINE SEARCH

The two optimization formulations (10) and (15) have the same state equations as follows:

$$\begin{cases} \boldsymbol{T}(\boldsymbol{u}) = \lambda \boldsymbol{f}_0 \\ \boldsymbol{f}_0^{\mathrm{T}} \boldsymbol{u} = 2C_0. \end{cases} \tag{20}$$

Finding a solution of the state equations (20) is equivalent to solving the equality-constrained minimization problem as follows:

$$\begin{cases} \min_{\boldsymbol{u}} \quad U(\boldsymbol{u}) \\ \text{s.t.} \quad \boldsymbol{f}_0^T \boldsymbol{u} = 2C_0. \end{cases} \tag{21}$$

We solve (21) using Newton's method with a backtracking line search strategy. We start with the Lagrangian function

$$\mathcal{L}(\boldsymbol{u}, \lambda) = U(\boldsymbol{u}) + \lambda \left(2C_0 - \boldsymbol{f}_0^T \boldsymbol{u}\right), \tag{22}$$

where λ is the Lagrangian multiplier, which is also the load factor in Equation (20). According to the Karush-Kuhn-Tucker optimality conditions, we obtain

$$\begin{cases} \frac{\partial \mathcal{L}}{\partial \boldsymbol{u}}(\boldsymbol{u}^*, \lambda^*) = \nabla U(\boldsymbol{u}^*) - \lambda^* \boldsymbol{f}_0 = 0 \\ \frac{\partial \mathcal{L}}{\partial \lambda}(\boldsymbol{u}^*, \lambda^*) = 2C_0 - \boldsymbol{f}_0^T \boldsymbol{u}^* = 0. \end{cases} \tag{23}$$

4.1 | Newton's method

At iteration k, we interpret the Newton step $\Delta \boldsymbol{u}_k$, and the associated multiplier λ_{k+1}, as the solutions of a linearized approximation of the optimality conditions in (23). We substitute $\boldsymbol{u}_k + \Delta \boldsymbol{u}_k$ for $\boldsymbol{u}^*$ and λ_{k+1} for λ^* and replace the gradient by its linearized approximation near $\boldsymbol{u}_k$, to obtain the equations

$$\begin{cases} \nabla U(\boldsymbol{u}_k + \Delta \boldsymbol{u}_k) - \lambda_{k+1}\boldsymbol{f}_0 \approx \nabla U(\boldsymbol{u}_k) + \nabla \nabla^T U(\boldsymbol{u}_k) \Delta \boldsymbol{u}_k - \lambda_{k+1}\boldsymbol{f}_0 = 0 \\ 2C_0 - \boldsymbol{f}_0^T (\boldsymbol{u}_k + \Delta \boldsymbol{u}_k) = 0. \end{cases} \tag{24}$$

Since $\nabla \nabla^T U(\boldsymbol{u}_k) = \boldsymbol{K}_T(\boldsymbol{u}_k)$ and $\nabla U(\boldsymbol{u}_k) = \boldsymbol{T}(\boldsymbol{u}_k)$, then (24) becomes

$$\begin{cases} \boldsymbol{T}(\boldsymbol{u}_k) + \boldsymbol{K}_T(\boldsymbol{u}_k) \Delta \boldsymbol{u}_k - \lambda_{k+1}\boldsymbol{f}_0 = 0 \\ 2C_0 - \boldsymbol{f}_0^T (\boldsymbol{u}_k + \Delta \boldsymbol{u}_k) = 0. \end{cases} \tag{25}$$

Solving for $\Delta \boldsymbol{u}_k$ using the first equation in system (25), we obtain

$$\Delta \boldsymbol{u}_k = \boldsymbol{K}_T^{-1}(\boldsymbol{u}_k) \left[-\boldsymbol{T}(\boldsymbol{u}_k) + \lambda_{k+1}\boldsymbol{f}_0\right]. \tag{26}$$

By means of the equality $\boldsymbol{f}_0^T \boldsymbol{u}_k = 2C_0$, the second equation in system (25) becomes

$$\boldsymbol{f}_0^T \Delta \boldsymbol{u}_k = 0. \tag{27}$$

Substituting Equation (26) into (27) and solving for λ_{k+1}, we obtain

$$\lambda_{k+1} = \frac{\boldsymbol{f}_0^T \Delta \boldsymbol{u}_k'}{\boldsymbol{f}_0^T \Delta \boldsymbol{u}_k''}, \Delta \boldsymbol{u}_k' = \boldsymbol{K}_T^{-1}(\boldsymbol{u}_k) \boldsymbol{T}(\boldsymbol{u}_k), \Delta \boldsymbol{u}_k'' = \boldsymbol{K}_T^{-1}(\boldsymbol{u}_k)\boldsymbol{f}_0. \tag{28}$$

TABLE 1 Newton's algorithm for solving nonlinear state equations

Algorithm 1 Newton's method for solving the nonlinear equations
Input: ρ, C_0, $\boldsymbol{f}_0$, *tol*.
Output: Solution λ and $\boldsymbol{u}$;
1: $\boldsymbol{u}_0' :=$ zeros (size($\boldsymbol{f}_0$)); $\boldsymbol{K}_0 \leftarrow$ Global stiffness matrix $[\rho, \boldsymbol{u}_0']$; $\boldsymbol{u}_0'' := \boldsymbol{K}_0 \backslash \boldsymbol{f}_0$;
2: $\boldsymbol{u}_0 := \frac{2C_0 \boldsymbol{u}_0''}{\boldsymbol{f}_0^T \boldsymbol{u}_0''}$
3: **for** $k = 0, 1, \ldots$, until convergence
4:   $\boldsymbol{T}_k \leftarrow$ Internal force vector $[\rho, \boldsymbol{u}_k]$;
5:   $\boldsymbol{K}_k \leftarrow$ Global stiffness matrix $[\rho, \boldsymbol{u}_k]$; $\beta := 10^{-8} \times$ mean(diag($\boldsymbol{K}_k$));
6:   $\boldsymbol{K}_k := \boldsymbol{K}_k + \beta \times$ sparse(identity(size($\boldsymbol{K}_k$)));
7:   $\Delta \boldsymbol{u}_k' := \boldsymbol{K}_k \backslash \boldsymbol{T}_k$; $\Delta \boldsymbol{u}_k'' := \boldsymbol{K}_k \backslash \boldsymbol{f}_0$;
8:   $\lambda_{k+1} := \frac{\boldsymbol{f}_0^T \Delta \boldsymbol{u}_k'}{\boldsymbol{f}_0^T \Delta \boldsymbol{u}_k''}$;
9:   $\Delta \boldsymbol{u}_k := -\Delta \boldsymbol{u}_k' + \lambda_{k+1} \Delta \boldsymbol{u}_k''$;
10:   Find step size α_k by an inexact line-search strategy (see **Algorithm 2**);
11:   $\boldsymbol{u}_{k+1} := \boldsymbol{u}_k + \alpha_k \Delta \boldsymbol{u}_k$;
12:   **if** $\frac{\|\Delta \boldsymbol{u}_k\|}{1 + \|\boldsymbol{u}_{k+1}\|} <$ *tol* or $\frac{\|\boldsymbol{T}_k - \lambda_k \boldsymbol{f}_0\|}{\|\boldsymbol{f}_0\|} <$ *tol* **then break**;
13:     **end if**
14: **end for**
15: $\lambda := \lambda_{k+1}$; $\boldsymbol{u} := \boldsymbol{u}_{k+1}$;

By substituting the expression of λ_{k+1} in Equation (28) into (26), we finally obtain the expression of the Newton step $\Delta \boldsymbol{u}_k$ as

$$\Delta \boldsymbol{u}_k = -\Delta \boldsymbol{u}_k' + \lambda_{k+1} \Delta \boldsymbol{u}_k''. \tag{29}$$

The detailed algorithm for Newton's method, as employed in the present work, is provided in Table 1. Based on the limit load concept, the stiffness matrix might become singular near the limit state, which can cause numerical difficulties. To prevent the possibility of a singular stiffness matrix, we add a Tikhonov regularization[21,22] parameter β into the tangent stiffness matrix, as shown in lines 4 and 5 of Table 1. Through the numerical examples, we verify that the Tikhonov regularization technique is effective.

4.2 | Inexact line-search approach

We utilize a mixed inexact line-search approach within Newton's method to improve the convergence of solving the nonlinear state equations. At iteration k, we obtain the Newton step $\Delta \boldsymbol{u}_k$ (ie, the descent direction) from (29). The technique of line search addresses the selection of the step size α_k for the iteration update

$$\boldsymbol{u}_{k+1} = \boldsymbol{u}_k + \alpha_k \Delta \boldsymbol{u}_k. \tag{30}$$

Given $\boldsymbol{u}_k$ and a descent direction $\Delta \boldsymbol{u}_k$, we choose the step size α_k such that

$$U(\boldsymbol{u}_{k+1}) = U(\boldsymbol{u}_k + \alpha_k \Delta \boldsymbol{u}_k) \leq U(\boldsymbol{u}_k) + \eta \alpha_k \nabla U(\boldsymbol{u}_k)^T \Delta \boldsymbol{u}_k, \tag{31}$$

where η is a guard constant, eg, $\eta = 10^{-4}$. In general, we start with $\tilde{\alpha}_k = 1$ and decrease it by a scale κ, ie, $\alpha_k = \kappa \tilde{\alpha}_k$ $(0 < \kappa < 1)$, until (31) is satisfied. In this study, we adopt an inexact line-search approach.[23] Let us define the function Φ in terms of α_k alone as

$$\Phi(\alpha) = U(\boldsymbol{u}_k + \alpha_k \Delta \boldsymbol{u}_k). \tag{32}$$

Since we know $\Phi(0) = U(\boldsymbol{u}_k)$, $\Phi'(0) = \nabla U(\boldsymbol{u}_k)^T \Delta \boldsymbol{u}_k$, and $\Phi(\tilde{\alpha}_k) = U(\boldsymbol{u}_k + \tilde{\alpha}_k \Delta \boldsymbol{u}_k)$, where $\tilde{\alpha}_k$ is the current and unsatisfactory step size, we can build a quadratic polynomial using these three data points as follows:

$$\Phi(\alpha) = \Phi(0) + \Phi'(0)\alpha + \frac{\left(\Phi(\tilde{\alpha}_k) - \Phi(0) - \Phi'(0)\tilde{\alpha}_k\right)}{\tilde{\alpha}_k^2} \alpha^2. \tag{33}$$

TABLE 2 Algorithm of a mixed inexact line-search algorithm[23]

Algorithm 2 Inexact line-search approach
Input: u_k, Δu_k
Output: step length α_k
1: $\alpha_{\max} := 1$; $\alpha_{\min} := 10^{-9}$; $\eta = 10^{-4}$;
2: $\alpha_k := \alpha_{\max}$; $u_{k+1} := u_k + \alpha_k \Delta u_k$;
3: **while** $U(u_{k+1}) > U(u_k) + \eta \alpha_k \nabla U(u_k)^T \Delta u_k$ **and** $\alpha_k > \alpha_{\min}$ **do**
4:     $\kappa := -\dfrac{\nabla U(u_k)^T \Delta u_k \alpha_k}{2\left(U(u_k + \tilde{\alpha}_k \Delta u_k) - U(u_k) - \nabla U(u_k)^T \Delta u_k \alpha_k\right)}$
5:     **if** $\kappa < 0.1$ **then**
6:         $\kappa := 0.5 \leftarrow$ Do not use quadratic interpolation
7:     **end if**
8:     $\alpha_k := \kappa \times \alpha_k$;
9: $u_{k+1} := u_k + \alpha_k \Delta u_k$;
10: **end while**
11: Return α_k

By minimizing the quadratic interpolant (33) with respect to α, we obtain

$$\frac{d\Phi(\alpha)}{d\alpha} = \Phi'(0) + \frac{2\left(\Phi(\tilde{\alpha}_k) - \Phi(0) - \Phi'(0)\tilde{\alpha}_k\right)}{\tilde{\alpha}_k^2}\alpha = 0. \tag{34}$$

From (34), we obtain the step size α_k as follows:

$$\begin{aligned}
\alpha_k &= -\frac{\Phi'(0)\tilde{\alpha}_k^2}{2\left(\Phi(\tilde{\alpha}_k) - \Phi(0) - \Phi'(0)\tilde{\alpha}_k\right)} \\
&= -\frac{\nabla U(u_k)^T \Delta u_k \tilde{\alpha}_k}{2\left(U(u_k + \tilde{\alpha}_k \Delta u_k) - U(u_k) - \nabla U(u_k)^T \Delta u_k \tilde{\alpha}_k\right)}\tilde{\alpha}_k = \kappa \tilde{\alpha}_k.
\end{aligned} \tag{35}$$

If the obtained factor κ is relatively small, eg, $\kappa < 0.1$, then we do not employ the quadratic interpolation in (33), and we simply choose $\kappa = 0.5$. The detailed algorithm for a mixed inexact line-search approach is provided in Table 2.

5 | VERIFICATION: INTERNALLY PRESSURIZED CYLINDER

The FEM approach (in terms of solving the nonlinear state equations) is verified in this section. The verification addresses the mechanical behavior of a long thick-walled cylinder subjected to internal pressure. This problem is one of the standard benchmark examples of elastic-plastic behavior and has been discussed extensively by Hill[24] and Prager and Hodge.[25] The accuracy and the robustness of the proposed approach are assessed by comparing the numerical results and the analytical solution.

The problem, shown in Figure 4, consists of a cylinder of inner radius, a, and outer radius, b, that is subjected to internal pressure, p, which increases gradually until a limit load (ie, collapse load) is reached. The cylinder is made of an elastic-perfectly plastic material that can be modeled using a von Mises criterion. Plane strain conditions are considered. Hill[24] derived the analytical solution of this problem to be

$$p_{\lim} = \frac{2\sigma_y}{\sqrt{3}}\ln\left(\frac{b}{a}\right), \tag{36}$$

where $p_{\lim}$ is the limit pressure and σ_y is the uniaxial yield stress.

In the numerical simulation, the nonlinear elastic constitutive model proposed in Section 2 is used to define the material. Due to symmetry, only a quarter of the cylinder cross section is considered with symmetry boundary conditions. Aside from the reference strain, the material properties listed in Table 3 are from the book by de Souza Neto et al.[27]

Figure 5 shows the internal pressure versus the prescribed energy obtained from the present finite element simulation together with the analytical solution. A comparison between numerical and analytical results is presented in Table 4, which shows that both results are in excellent agreement with error magnitude less than 0.3%.
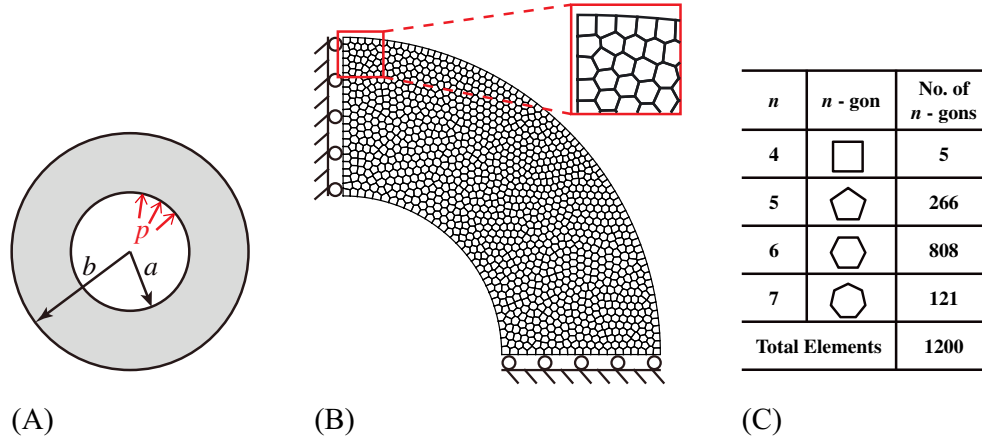
FIGURE 4 A, Geometry, boundary conditions, and mesh discretization of the internally pressurized cylinder problem; B, A quarter of the domain is discretized by 1200 polygonal finite elements under plane strain conditions[26]; C, Composition of the polygonal mesh [Colour figure can be viewed at wileyonlinelibrary.com]

TABLE 3 Material properties and dimension used in the internally pressurized cylinder problem

Property	Symbol	Magnitude (de Souza Neto et al[27])
Young's modulus	E	2.1×10^5 MPa
Poisson's ratio	υ	0.3
Uniaxial yield stress	σ_y	240 MPa
Reference strain	ε_{ref}	0.0001
Inner radius	a	100 mm
Outer radius	b	200 mm
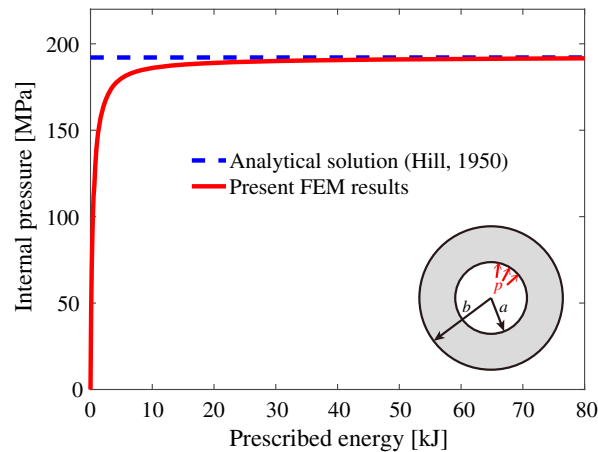
FIGURE 5 Internally pressurized cylinder problem. Comparison between the present numerical solution and the analytical solution. FEM, finite element method [Colour figure can be viewed at wileyonlinelibrary.com]

TABLE 4 Comparison between the numerical and analytical solutions for the internally pressurized cylinder problem

Reference Strain ε_{ref}	Numerical (MPa)	Analytical (MPa) Equation (36)	Error %
0.0001	191.5980	192.0906	−0.26

TABLE 5 Influence of the inexact line-search approach

Newton's Method *With Line Search*			Newton's Method *Without Line Search*
FEM iter.	Step Size	$\frac{\|\Delta u\|}{1+\|u\|}$	
1	1.00	3.99×10^{-1}	
2	6.35×10^{-2}	1.22×10^{-1}	
3	6.91×10^{-2}	9.84×10^{-2}	
4	8.43×10^{-2}	8.37×10^{-2}	
5	1.26×10^{-1}	7.89×10^{-2}	
6	1.13×10^{-1}	3.56×10^{-2}	
7	1.96×10^{-1}	3.86×10^{-2}	No convergence
8	1.00	9.04×10^{-2}	
9	1.00	3.08×10^{-2}	
10	1.00	5.40×10^{-3}	
11	1.00	4.60×10^{-3}	
12	1.00	1.47×10^{-3}	
13	1.00	4.32×10^{-4}	
14	9.31×10^{-10}	2.38×10^{-14}	

Abbreviation: FEM, finite element method.

In order to demonstrate the influence of the line search method (described in Section 4.2), we solve the cylinder problem using Newton's method with and without line search. The nonlinear FEM iterations are shown in Table 5. The case with the line search approach converges within 14 FEM iterations, whereas the case without the line search fails to converge. Thus, this example highlights the relevance of the line search method.

6 | NUMERICAL EXAMPLES

Four numerical examples demonstrate the key features of the present formulations for material nonlinear topology optimization considering the von Mises criterion. A summary of the examples is provided in Table 6.

TABLE 6 Brief description of the numerical examples

Example	Description	Remarks
1	Three-supports beam (Maute et al[3])	• Optimized topologies agree with those from the literature • Results obtained from max strain energy are similar to those from max load factor • Poisson's ratio, $\upsilon = 0$ (from Maute et al[3])
2	Clamped beam	• Assuming small strain, we obtain the topology that was obtained considering finite strain plasticity by Wallin et al[10] • Convergence plot for max U formulation exhibits smooth behavior • Poisson's ratio, $\upsilon = 0$
3	Structural performance of the optimized clamped beams	• Verification of topologically optimized structures using commercial FEA software • Comparison of structural performance using Mises plasticity and those considering the nonlinear elastic model • Poisson's ratio, $\upsilon = 0$
4	Three fixed-sides beam	• Nonzero Poisson's ratio, $\upsilon = 0.26$ • Investigation of the nonlinear solutions considering two reference strains (ie, $\varepsilon_{ref} = 0.002$ and $\varepsilon_{ref} = 0.0004$)

Abbreviation: FEA, finite element analysis.

6.1 | Three-support beam

We first present the three-support beam example to illustrate the behavior of the proposed nonlinear topology optimization framework for approximating plasticity. In order to compare the present numerical simulation with the results in the literature, we use the same geometry, boundary conditions, material properties, and volume fraction used by Maute et al.[3] Figure 6 shows the geometry and dimensions of the three-support beam problem. A distributed load with magnitude of $w = 6$ kN/m is applied on a 4-m portion of the top of the beam. The material properties are listed in Table 7. In the present numerical simulation, we use the proposed nonlinear elastic material constitutive model, as illustrated in Figure 7. We choose the reference strain as 0.0005. The domain is discretized with 7200 quadrilateral elements under plane strain conditions. We use the solid isotropic material with penalization (SIMP) model[28-30] with the constant penalty parameter as 3. As usual, the SIMP design problem is solved by the optimality criteria approach, together with the density filter[31,32] strategy. The linear density filter radius used in this example is equal to 0.4167.

Figure 8 shows the optimized topologies and the related von Mises stress distribution plots obtained using the formulation for maximizing the strain energy (max U). The scale of the stress contour is between 0 and 1, with 1 representing the stress state reaching the von Mises yielding limit. When the prescribed energy C_0 is 10^{-4} kJ, the optimized topology and the related von Mises stress distribution contour are shown in Figure 8A. The stress contour shows that when the prescribed energy is relatively small, the entire structure is in the linear elastic range. When the prescribed energy C_0
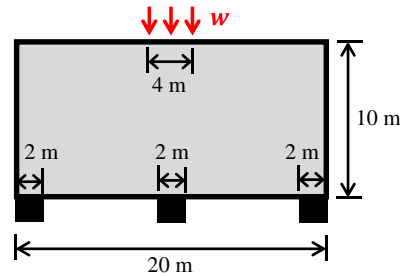

FIGURE 6 Geometry, loading, and support conditions of the three-support beam problem [Colour figure can be viewed at wileyonlinelibrary.com]

TABLE 7 Material properties used in the three-support beam problem

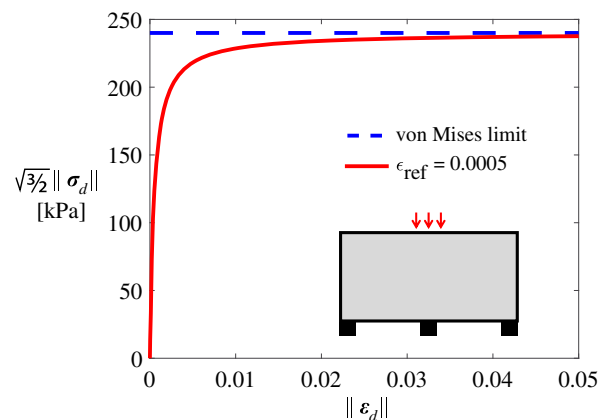| Property	Symbol	Magnitude(Maute et al[3])
Young's modulus	E	3×10^4 kPa
Poisson's ratio	υ	0
Uniaxial yield stress	σ_y	240 kPa
Volume fraction	$\overline{v}$	30%

FIGURE 7 Illustration of the nonlinear elastic material constitutive model used in the three-support beam problem [Colour figure can be viewed at wileyonlinelibrary.com]
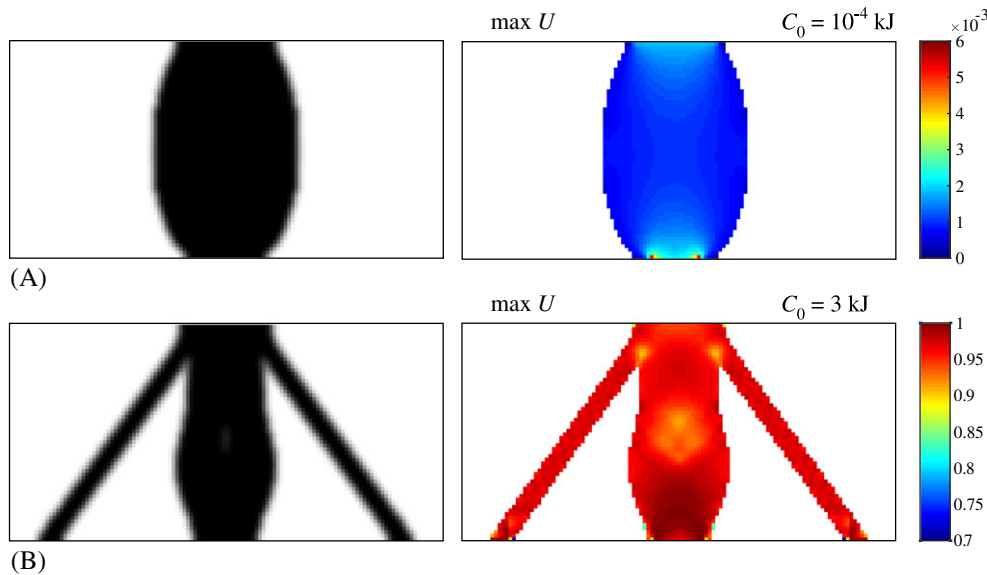
FIGURE 8   Results of the three-support beam problem obtained from the max U formulation. The optimized topology and the related von Mises stress distribution considering (A) $C_0 = 10^{-4}$ kJ and (B) $C_0 = 3$ kJ. The scale of the von Mises stress contour is between 0 and 1, with 1 representing the stress state reaching the von Mises yielding limit

is 3 kJ, the optimized topology and the related von Mises stress distribution contour are shown in Figure 8B. The contour plot shows that when the prescribed energy is relatively high, the entire structure is almost plastified. The optimized topology of Figure 8B agrees with the result by Maute et al.[3] If the prescribed energy is more than 3 kJ, we obtain the same optimized topology as the one shown in Figure 8B.

Figure 9 shows the optimized topologies and the related von Mises stress distribution plots obtained using the formulation of maximizing the load factor (max λ), which has a similar behavior to the max U results described in the previous paragraph. Notice that since the max λ formulation is not self-adjoint, the sign of sensitivities in Equation (19) can be negative. In this three-support beam problem, the maximal order of magnitude of negative sensitivities is -4.

Table 8 lists the quantitative comparison of results obtained from the two formulations in the three-support beam problem. When the prescribed energy is relatively small (ie, the structure is in the linear elastic range), the strain energy and reaction load factor obtained from both formulations are exactly the same. When the prescribed energy is relatively
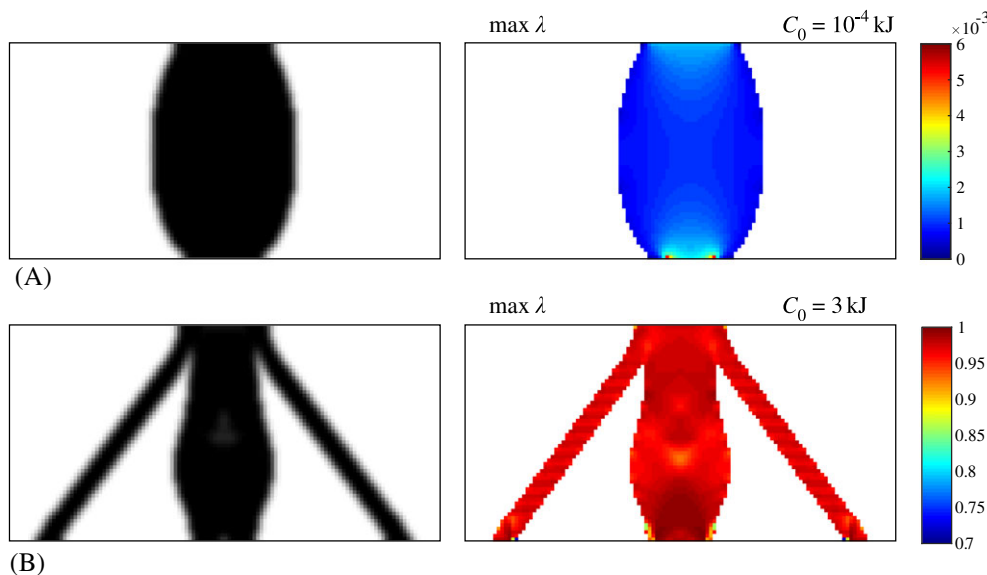

FIGURE 9   Results of the three-support beam problem obtained from the max λ formulation. The optimized topology and the related von Mises stress distribution considering (A) $C_0 = 10^{-4}$ kJ and (B) $C_0 = 3$ kJ. The scale of the von Mises stress contour is between 0 and 1, with 1 representing the stress state reaching the von Mises yielding limit

TABLE 8 Quantitative comparison of results obtained from the two formulations (ie, max strain energy and max load factor) in the three-support beam problem

C_0(kJ)	Formulation			
	max U		max λ	
	U (kJ)	λ	U (kJ)	λ
10^{-4}	3.7057×10^{-6}	0.0370	3.7057×10^{-6}	0.0370
3	242.3085	48.2739	240.3609	48.6612

large (ie, the structure is in the nonlinear range), the two formulations give very similar results. The strain energy obtained from the max U formulation is only slightly larger than that obtained from the max λ formulation. The reaction load factor obtained from the max λ formulation is slightly larger than that obtained from the max U.

6.2 | Clamped beam

The clamped beam example is a benchmark problem used to illustrate the behavior of the proposed nonlinear topology optimization framework considering the von Mises criterion. In order to compare the present numerical simulation with the results in the literature, we use the same geometry, boundary conditions, and material properties proposed by Maute et al.[3] Figure 10 shows the geometry and dimensions of the clamped beam problem. The beam is fixed at both left and right ends. A distributed load with magnitude of $w = 100$ kN/m is applied on a 2.5-m portion of the top of the beam. The material properties are listed in Table 9. In the present numerical simulation, we use the nonlinear elastic material constitutive model illustrated in Figure 11. We choose the small reference strain as 0.0005. The domain is discretized with 6400 quadrilateral elements under plane strain conditions. The linear filter radius used in this example is equal to 0.16. We use the SIMP model with the constant penalty parameter as 3.

Figure 12 shows the optimized topologies and the related von Mises stress distribution plots obtained using the formulation for maximizing the strain energy. When the prescribed energy $C_0 = 10^{-3}$ kJ, the optimized topology and related von Mises stress distribution contours are shown in Figure 12A. The contour shows that the entire structure is in the linear elastic range. When the prescribed energy $C_0 = 35$ kJ, the optimized topology and the related von Mises stress distribution contour are shown in Figure 12B. The contour plot in Figure 12B shows that the entire structure is almost plastified. The topology shown in Figure 12B agrees with the result by Maute et al.[3] When the prescribed energy $C_0 = 63$ kJ, we obtain another optimized topology as shown in Figure 12C. The contour plot in Figure 12C shows that almost the entire structure reaches the limit of von Mises stress. Although the numerical simulations are performed under a small-deformation
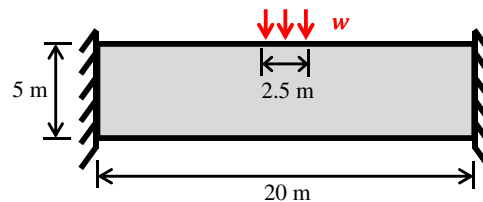

FIGURE 10 Geometry, loading, and support conditions of the clamped beam problem [Colour figure can be viewed at wileyonlinelibrary.com]

TABLE 9 Material properties used in the clamped beam problem

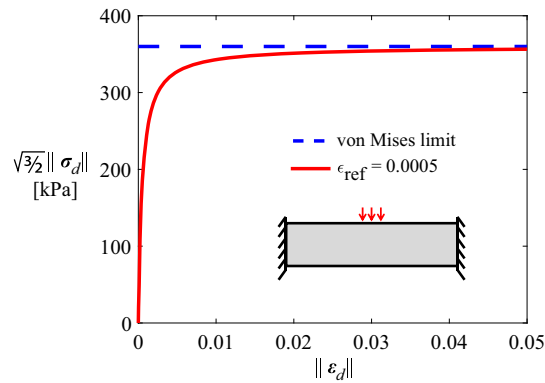| Property	Symbol	Magnitude (Maute et al[3])
Young's modulus	E	1.8×10^5 kPa
Poisson's ratio	υ	0
Uniaxial yield stress	σ_y	360 kPa
Volume fraction	$\bar{v}$	25%

FIGURE 11 Illustration of the nonlinear elastic material constitutive model utilized in the clamped beam problem [Colour figure can be viewed at wileyonlinelibrary.com]
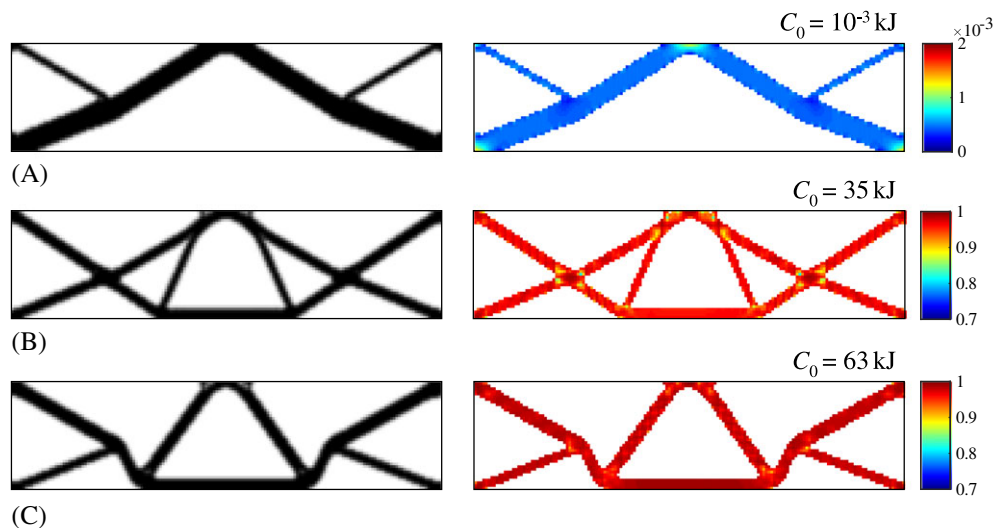

FIGURE 12 Results of the clamped beam problem obtained from the max U formulation. The optimized topologies and related von Mises stress distributions considering (A) $C_0 = 10^{-3}$ kJ, (B) $C_0 = 35$ kJ, and (C) $C_0 = 63$ kJ. The scale of the von Mises stress contour is between 0 and 1, with 1 representing the stress state reaching the von Mises yielding limit

TABLE 10 Clamped beam problem. Results obtained from the max U formulation using different prescribed energy values C_0

C_0 (kJ)	U (kJ)	λ
10^{-3}	4.4694×10^{-7}	4.4702×10^{-4}
35	69.1166	1.1607
63	135.3912	1.1901

assumption, the topologies obtained using different prescribed energies are drastically distinct, as shown in Figure 12. The topology in Figure 12C is similar to the one obtained by Wallin et al[10] considering finite strain plasticity. Table 10 lists the results obtained from the max U formulations in the clamped beam problem. Similar results are obtained with the max λ formulation.

The proposed topology optimization framework considering the von Mises criterion has good convergence behavior. For example, Figure 13 illustrates the convergence history of the clamped beam problem using the max U formulation with the prescribed energy $C_0 = 35$ kJ. The intermediate topologies at iterations #15, #50, and #100 and the final optimized topology are shown in Figure 13. It is clear that the convergence curve is quite smooth. As stated earlier, path-dependent models often tend to display difficulty in convergence. Utilizing the present nonlinear elastic constitutive model, we can achieve optimization with promising convergence characteristics.
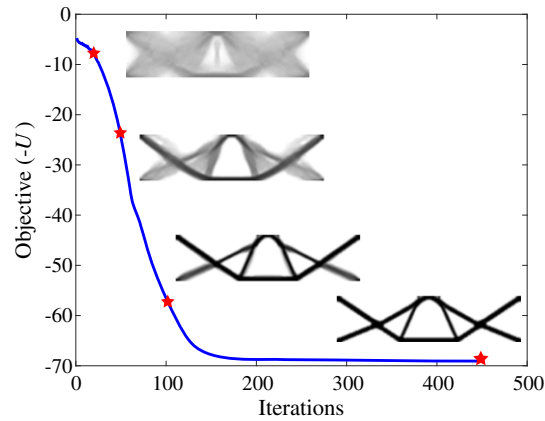
FIGURE 13 Convergence study of the clamped beam problem using the max U formulation with the prescribed energy $C_0 = 35$ kJ [Colour figure can be viewed at wileyonlinelibrary.com]

6.3 | Structural performance of three topology-optimized clamped beams

In this section, we verify the structural performance of the three topology-optimized clamped beam structures in ABAQUS composed of two different types of material constitutive models, namely, the built-in isotropic Mises plasticity model and the present asymptotic nonlinear elastic model (the UMAT file is provided in the work of Pasquali[13]).

At first, three optimized clamped beam structures are digitized and converted into CAD models in ABAQUS. To digitize the previously obtained beam structures into CAD models, we need high-resolution and clear boundaries of the optimized structures. Therefore, relatively fine meshes are used in solving the clamped beam problems in this section. Figure 14A-C shows the three topology-optimized structures with relatively high resolution. Due to symmetry, only half of the optimized structure is considered for analysis with symmetry boundary conditions. The optimized structure in Figure 14A is modeled with linear elastic material, whereas the other two optimized structures in Figure 14B,C use von Mises plastic material. The clear solid boundaries are defined by a cutoff (or threshold) value. Densities (ie, design variables) $\rho > cutoff = 0.5$ are considered to be solid.[33] This approach allows us to represent the boundaries of the optimized structures by contour lines while preserving the volume constraint. By generating contour lines with density $cutoff = 0.5$,
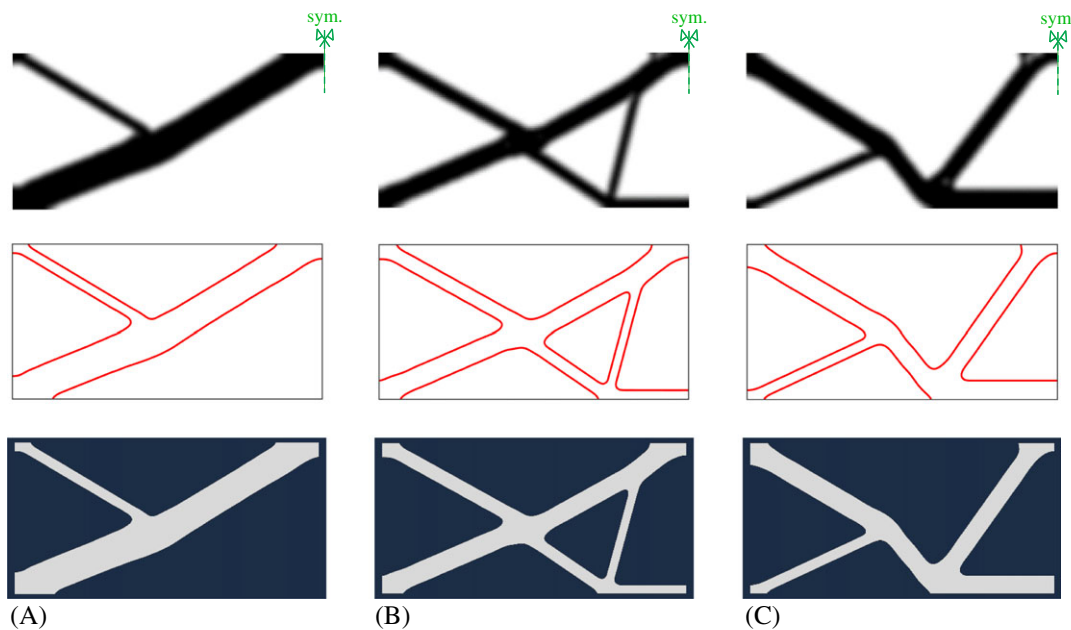

FIGURE 14 An optimized clamped beam structure considering (A) linear elastic material, (B) von Mises plastic material at stage 1, and (C) von Mises plastic material at stage 2. The first row shows the density field obtained from topology optimization. The second row shows contour lines using the density cutoff $\rho = 0.5$. The third row shows the digitized structures that are converted into a CAD model in ABAQUS. The corresponding topologies on the third row are named topologies I, II, and III, respectively [Colour figure can be viewed at wileyonlinelibrary.com]

the boundaries of the three optimized structures are clearly defined, as shown in Figure 14. Finally, the obtained contour lines are imported into AutoCAD as polylines and then exported as a standard ACIS file, which later can be imported into ABAQUS. Figure 14 shows the CAD model in ABAQUS, named as topologies I, II, and III. The volume values of topologies I, II, and III are 12.40, 12.46, and 12.39, respectively. Notice that the volume fraction is 25% (ie, the upper-bound volume is $5 \times 10 \times 25\% = 12.5$) in this optimization of the clamped beam problem. In ABAQUS, topologies I, II, and III are discretized by 67 414, 68 065, and 66 708 linear triangular elements of type CPE3, respectively, and analyzed under plane strain conditions. The material properties are defined as Young's modulus $E = 180\,000$ kPa, Poisson's ratio $v = 0$, and uniaxial yield stress $\sigma_y = 360$ kPa. The general static algorithm is used for solution under the prescribed pressure load.

Next, increasing pressure is applied on these beam structures until the magnitude of vertical displacement at point A (see Figure 15) reaches 0.1835 m. The structural performance of the three topologies is investigated with two different material constitutive models. In the first case, an elastic–perfectly plastic Mises model is used to define the material. Considering this classical Mises plasticity model, we obtain the behavior of the three topologies, shown as solid curves in Figure 15. Each curve represents the applied pressure versus the vertical displacement at point A of the clamped beam. A failure mechanism of those structures is discussed in Appendix C. In the second case, the present asymptotic nonlinear elastic model is used to define the material. When the reference strain (ε_{ref}) is 0.0005, the behavior of the three topologies is obtained, as shown by the dashed curves in Figure 15. In addition, the three dotted lines in Figure 15 present the behavior of the topologies considering $\varepsilon_{ref} = 0.0016$, where the consistent tangent matrix at the origin coincides with the linear elastic material model (see detailed derivation in Appendix A). The limit pressures for topologies I, II, and III considering different material constitutive models are listed in Table 11. We notice that the limit pressure obtained using the nonlinear elastic model is always lower than that obtained using the classical Mises plasticity model.

Lastly, the stress contours obtained using classical Mises plasticity are compared with those obtained using the nonlinear elastic model. Under limit pressures, the von Mises stress contours of topologies I, II, and III are shown in Figure 16.
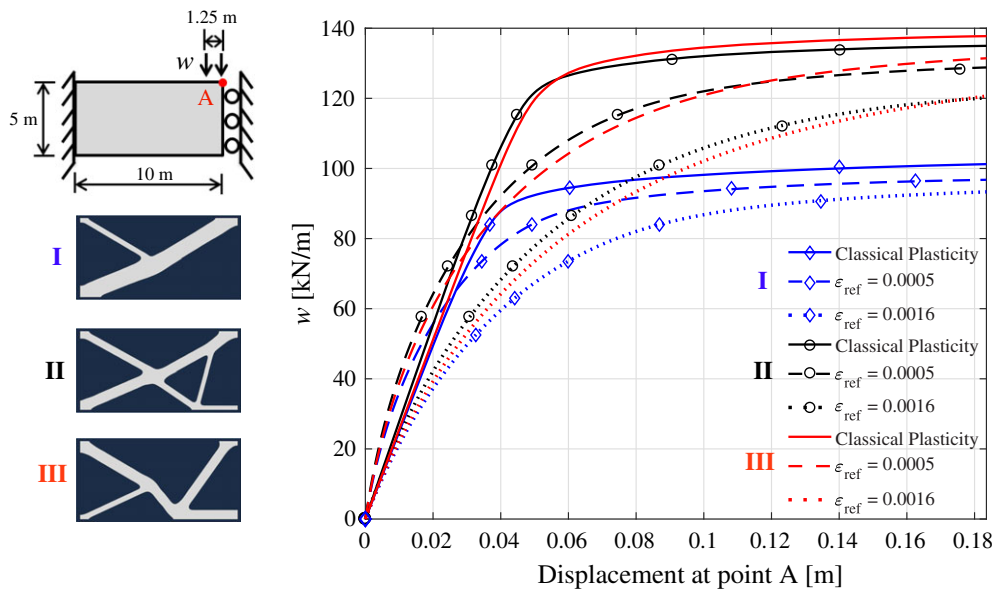

FIGURE 15 Structural performance of the three optimized topologies. The structures are loaded until the magnitude of vertical displacement at point A reaches 0.1835 m. Solid lines represent the structural behavior using the classical Mises plasticity. Dashed lines and dotted lines represent the structural behavior embedded with the user-defined nonlinear elastic model using $\varepsilon_{ref} = 0.0005$ and $\varepsilon_{ref} = 0.0016$, respectively [Colour figure can be viewed at wileyonlinelibrary.com]

TABLE 11 The limit load (w_{lim}) for topologies I, II, and III considering different material constitutive models

	Classical Mises Plasticity, kN/m	Nonlinear Elastic ($\varepsilon_{ref} = 0.0005$), kN/m	Nonlinear Elastic ($\varepsilon_{ref} = 0.0016$), kN/m
Topology I	101.3250	96.7641	93.4500
Topology II	135.0309	129.0600	120.9600
Topology III	137.8888	132.0000	123.0000

Classical Mises Plasticity   Nonlinear Elasticity
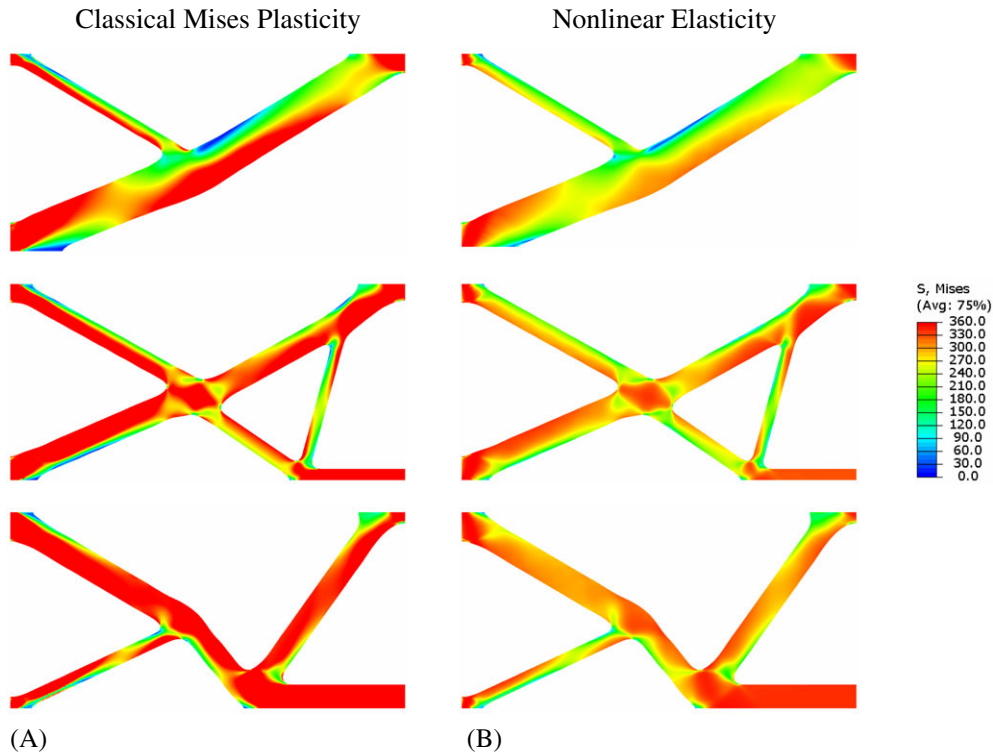

(A)   (B)

FIGURE 16   Under the limit pressure, von Mises stress contours of topologies I, II, and III obtained considering (A) the classical Mises plastic model and (B) the nonlinear elastic model ($\varepsilon_{\text{ref}} = 0.0005$)

The three contours in Figure 16A are obtained using classical Mises plasticity, and the contours in Figure 16B are obtained considering the nonlinear elastic model ($\varepsilon_{\text{ref}} = 0.0005$). From a qualitative point of view, the area of the red region (ie, plastified region) on the contour using the nonlinear elastic model is less than that on the contour considering the classical Mises plasticity model. Quantitatively, the stress state of the analysis using the nonlinear elastic model is always below the yielding surface (ie, at any point on the contours considering nonlinear elastic, the von Mises stress is less than the yield stress $\sigma_y = 360$ kPa). On the basis of the lower-bound theorem[14] in Appendix B, we conclude that the analysis considering the nonlinear elastic asymptotic material model provides a more conservative (ie, safer) design in terms of limit analysis.

6.4 | Three fixed-edges beam

In order to investigate how materials with realistic properties impact optimal designs, we present a beam problem with fixed boundary on three sides and distributed load ($w = 100$ MN/m) on the top. Two beams with different dimensions, as shown in Figure 17A,B, are investigated in this section. We consider a commonly used A36 steel with the material
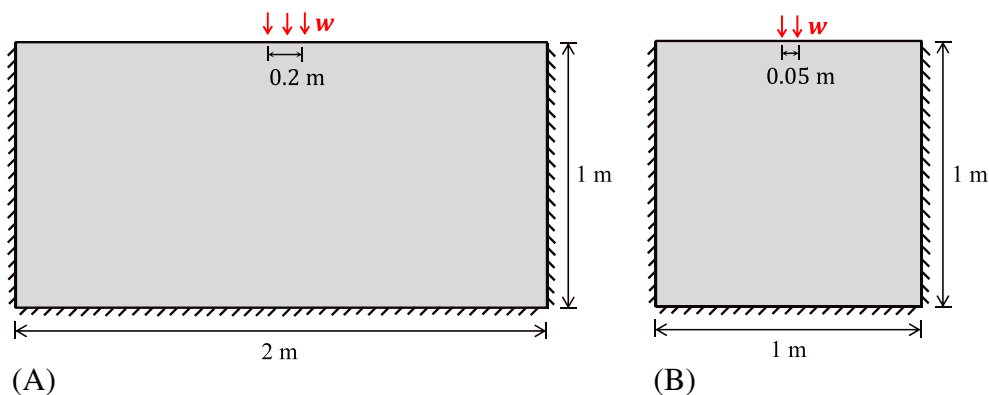

(A)   (B)

FIGURE 17   Two types of geometries for the beam problem with fixed boundary on three sides and distributed load on the top. A, 2 m × 1 m design domain; B, 1 m × 1 m design domain [Colour figure can be viewed at wileyonlinelibrary.com]

TABLE 12 Material properties (ie, A36 steel) used in the beam problem with three fixed edges

Property	Symbol	Magnitude
Young's modulus	E	2×10^5 MPa
Poisson's ratio	v	0.26
Uniaxial yield stress	σ_y	380 MPa
Reference strain	ε_{ref}	0.002 or 0.0004

properties shown in Table 12. We consider two small reference strains (ε_{ref}) 0.0004 and 0.002. For $\varepsilon_{\text{ref}} = 0.002$, the consistent tangent matrix is the same as the linear elastic case at the origin (see detailed derivation in Appendix A). Figure 18 illustrates the nonlinear elastic model considering $\varepsilon_{\text{ref}} = 0.002$ and $\varepsilon_{\text{ref}} = 0.0004$. Plane strain conditions are adopted.

We use quadrilateral elements to discretize the 2 m × 1 m and 1 m × 1 m design domains shown in Figure 17. Table 13 provides information such as the number of elements, volume fraction, linear density filter radius, and penalty parameter used in the numerical simulation for this problem. The max U formulation is used in the present study.

For the 2 m × 1 m design domain, the optimized topologies are shown in Figure 19. Figure 19A presents the optimized result considering the reference strain (ε_{ref}) as 0.002 and the small prescribed energy $C_0 = 10^{-6}$ MJ. This topology is identical to the linear elastic result obtained using the educational code PolyTop.[34] When the prescribed energy $C_0 = 0.4$ MJ, Figures 19B and 19C show the nonlinear solutions considering $\varepsilon_{\text{ref}} = 0.002$ and $\varepsilon_{\text{ref}} = 0.0004$, respectively. The topologies of the two nonlinear solutions are the same. The objectives (ie, strain energy U) of those solutions are compared in Table 14.

For the 1 m × 1 m design domain, Figure 20 presents the optimized solutions. The topology shown in Figure 20A is the same as the one obtained using PolyTop[34] considering a linear elastic material. Figure 20B,C illustrates the nonlinear solutions considering the same prescribed energy (C_0) but different reference strains (ε_{ref}). The topologies of the two nonlinear solutions are quite different. Table 14 includes the comparison of the objectives (U) for those solutions. Note that we use a filter-order continuation scheme to improve the quality of the nonlinear solution in Figure 20B. More details about the filter scheme is illustrated in Appendix D.
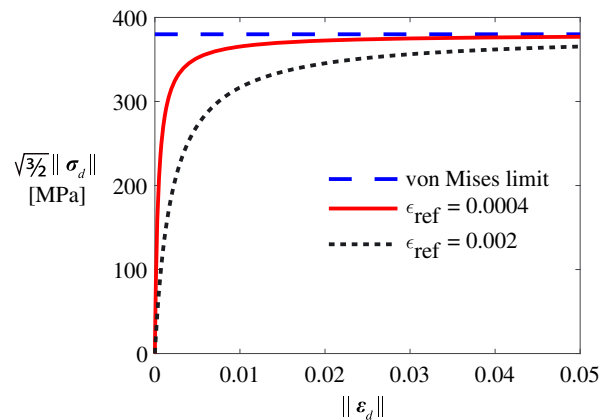
FIGURE 18 Illustration of the nonlinear elastic material constitutive model (with $\varepsilon_{\text{ref}} = 0.002$ and $\varepsilon_{\text{ref}} = 0.0004$) used in the beam problem with three fixed sides [Colour figure can be viewed at wileyonlinelibrary.com]

TABLE 13 Parameters used in the optimization of the three fixed-edges beam with two types of geometries (2 m × 1 m and 1m × 1m)

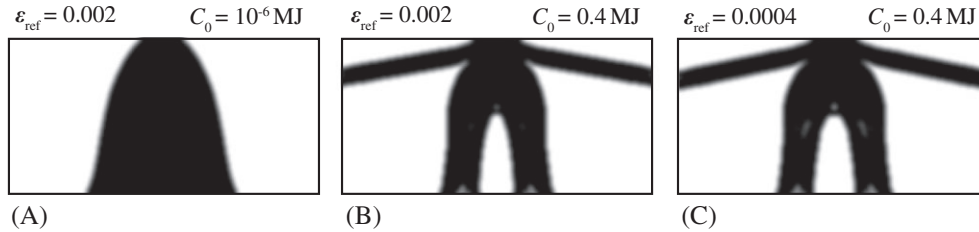|	2 m × 1 m Beam	1 m × 1 m Beam
No. of elements	20 000	22 500
Volume fraction	35%	20%
Filter radius	0.035	0.02
Constant penalty (p)	3	3

FIGURE 19 Results of the 2 m × 1 m, three fixed-edges beam obtained from the max U formulation. The optimized topologies considering (A) $\varepsilon_{\text{ref}} = 0.002$ and $C_0 = 10^{-6}$ MJ, (B) $\varepsilon_{\text{ref}} = 0.002$ and $C_0 = 0.4$ MJ, and (C) $\varepsilon_{\text{ref}} = 0.0004$ and $C_0 = 0.4$ MJ

TABLE 14 Results obtained from the max U formulation for the three fixed-edges beam problem

Design Domain	Case 1			Case 2			Case 3		
	ε_{ref}	C_0 [MJ]	U [MJ]	ε_{ref}	C_0 [MJ]	U [MJ]	ε_{ref}	C_0 [MJ]	U [MJ]
2 m × 1 m	0.002	10^{-6}	5×10^{-10}	0.002	0.4	6.7347	0.0004	0.4	7.4436
1 m × 1 m	0.002	10^{-6}	2×10^{-9}	0.002	0.1	1.8721	0.0004	0.1	1.9921
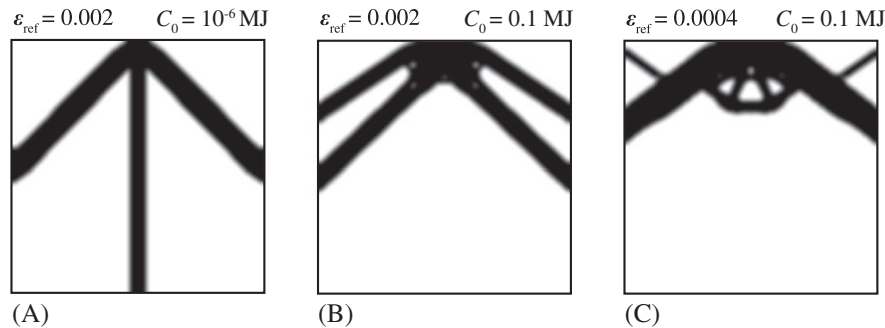
FIGURE 20 Results of the 1 m × 1 m, three fixed-edges beam obtained from the max U formulation. The optimized topologies considering (A) $\varepsilon_{\text{ref}} = 0.002$ and $C_0 = 10^{-6}$ MJ, (B) $\varepsilon_{\text{ref}} = 0.002$ and $C_0 = 0.1$ MJ, and (C) $\varepsilon_{\text{ref}} = 0.0004$ and $C_0 = 0.1$ MJ

7 | CONCLUSION

This paper addresses material nonlinear topology optimization problems considering the von Mises criterion by means of an asymptotic analysis using a fictitious nonlinear elastic model. With this asymptotic nonlinear elastic model, the sensitivity analysis is quite effective and efficient in the sense that there is no extra adjoint equation. The internally pressurized cylinder example illustrates that the plastic solution is equivalent to the nonlinear elastic solution in the limit stage. Two equivalent optimization formulations are presented: maximizing the structural strain energy (max U) and maximizing the load factor (max λ). We consider the topology optimization problem subjected to a certain prescribed energy—we prescribe the energy C_0 for all design cycles until an optimal design is reached. This prescribed energy approach leads to robust convergence in nonlinear problems. The nonlinear state equations are solved using direct minimization of the structural strain energy employing Newton's method with an inexact line-search strategy, which improves the convergence of the nonlinear FEM. Four numerical examples demonstrate the features of the approach. *The results are compared with those in the literature considering plasticity, in which very similar topologies are obtained*. In addition, we are able to obtain the optimized clamped beam structure (Figure 12), which can be found in the literature considering finite deformation.[10] We show that the material nonlinear topology optimization problem accounting for the von Mises criterion in numerical examples has smooth convergence when considering the nonlinear elastic formulation. Additionally, we obtain new nonlinear solutions (Figures 19 and 20) accounting for realistic plastic material properties (with nonzero Poisson's ratio), which can serve as benchmark problems.

ACKNOWLEDGEMENTS

ORCID

Glaucio H. Paulino https://orcid.org/0000-0002-3493-6857

REFERENCES

1. Yuge K, Kikuchi N. Optimization of a frame structure subjected to a plastic deformation. *Structural Optimization*. 1995;10(3-4):197-208.
2. Swan CC, Kosaka I. Voigt–Reuss topology optimization for structures with nonlinear material behaviors. *Int J Numer Methods Eng*. 1997;40(20):3785-3814.
3. Maute K, Schwarz S, Ramm E. Adaptive topology optimization of elastoplastic structures. *Structural Optimization*. 1998;15(2):81-91.
4. Schwarz S, Maute K, Ramm E. Topology and shape optimization for elastoplastic structural response. *Comput Methods Appl Mech Eng*. 2001;190(15-17):2135-2155.
5. Yoon GH, Kim YY. Topology optimization of material-nonlinear continuum structures by the element connectivity parameterization. *Int J Numer Methods Eng*. 2007;69(10):2196-2218.
6. Bogomolny M, Amir O. Conceptual design of reinforced concrete structures using topology optimization with elastoplastic material modeling. *Int J Numer Methods Eng*. 2012;90(13):1578-1597.
7. James KA, Waisman H. Failure mitigation in optimal topology design using a coupled nonlinear continuum damage model. *Comput Methods Appl Mech Eng*. 2014;268:614-631.
8. Kato J, Hoshiba H, Takase S, Terada K, Kyoya T. Analytical sensitivity in topology optimization for elastoplastic composites. *Struct Multidiscip Optim*. 2015;52(3):507-526.
9. Nakshatrala PB, Tortorelli DA. Topology optimization for effective energy propagation in rate-independent elastoplastic material systems. *Comput Methods Appl Mech Eng*. 2015;295:305-326.
10. Wallin M, Jönsson V, Wingren E. Topology optimization based on finite strain plasticity. *Struct Multidiscip Optim*. 2016;54(4):783-793.
11. Xia L, Fritzen F, Breitkopf P. Evolutionary topology optimization of elastoplastic structures. *Struct Multidiscip Optim*. 2017;55(2):569-581.
12. Alberdi R, Khandelwal K. Topology optimization of pressure dependent elastoplastic energy absorbing structures with material damage constraints. *Finite Elem Anal Des*. 2017;133:42-61.
13. Pasquali PRZ. *Análise Limite de Estruturas Através de Uma Formulação em Elasticidade Não-Linear* [master's thesis]. Porto Alegre, Brazil: Universidade Federal do Rio Grande do Sul; 2008.
14. Chen W-F, Han D-J. *Plasticity for Structural Engineers*. Plantation, FL: J. Ross Publishing; 2007.
15. Crisfield MA. *Non-Linear Finite Element Analysis of Solids and Structures*. Vol. 1. New York, NY: Wiley; 1991.
16. Mises RV. Mechanik der festen Körper im plastisch-deformablen Zustand. *Nachrichten von der Gesellschaft der Wissenschaften zu Göttingen, Mathematisch-Physikalische Klasse*. 1913;1913:582-592.
17. Christensen PW, Klarbring A. *An Introduction to Structural Optimization*. Vol. 153. Berlin, Germany: Springer Science & Business Media; 2008.
18. Bendsøe MP, Sigmund O. *Topology Optimization: Theory, Methods, and Applications*. Berlin, Germany: Springer-Verlag Berlin Heidelberg; 2003.
19. Niu F, Xu S, Cheng G. A general formulation of structural topology optimization for maximizing structural stiffness. *Struct Multidiscip Optim*. 2011;43(4):561-572.
20. Klarbring A, Strömberg N. Topology optimization of hyperelastic bodies including non-zero prescribed displacements. *Struct Multidiscip Optim*. 2013;47(1):37-48.
21. Tikhonov AN, Arsenin VY. *Solving Ill-Posed Problems*. New York, NY: John Wiley and Sons, Inc; 1977.
22. Ramos AS, Paulino GH. Filtering structures out of ground structures-a discrete filtering tool for structural design optimization. *Struct Multidiscip Optim*. 2016;54(1):95-116.
23. Ascher UM, Greif C. *A First Course in Numerical Methods*. Vol. 7. Philadelphia, PA: Society for Industrial and Applied Mathematics (SIAM); 2011.
24. Hill R. *The Mathematical Theory of Plasticity*. Vol. 11. Oxford, UK: Oxford University Press; 1998.
25. Prager W, Hodge PG. *Theory of Perfectly Plastic Solids*. New York, NY: John Wiley & Sons; 1951.
26. Talischi C, Paulino GH, Pereira A, Menezes IF. PolyMesher: a general-purpose mesh generator for polygonal elements written in MATLAB. *Struct Multidiscip Optim*. 2012;45(3):309-328.
27. de Souza Neto EA, Peric D, Owen DRJ. *Computational Methods for Plasticity: Theory and Applications*. Hoboken, NJ: John Wiley & Sons; 2011.

28. Bendsøe MP. Optimal shape design as a material distribution problem. *Structural Optimization*. 1989;1(4):193-202.

29. Rozvany GI. A critical review of established methods of structural topology optimization. *Struct Multidiscip Optim*. 2009;37(3):217-237.

30. Rozvany GI, Zhou M, Birker T. Generalized shape optimization without homogenization. *Structural Optimization*. 1992;4(3-4):250-252.

31. Bourdin B. Filters in topology optimization. *Int J Numer Methods Eng*. 2001;50(9):2143-2158.

32. Borrvall T, Petersson J. Topology optimization using regularized intermediate density control. *Comput Methods Appl Mech Eng*. 2001;190(37-38):4911-4928.

33. Zegard T, Paulino GH. Bridging topology optimization and additive manufacturing. *Struct Multidiscip Optim*. 2016;53(1):175-192.

34. Talischi C, Paulino GH, Pereira A, Menezes IF. PolyTop: a MATLAB implementation of a general topology optimization framework using unstructured polygonal finite element meshes. *Struct Multidiscip Optim*. 2012;45(3):329-357.

35. Cook RD, Malkus DS, Plesha ME, Witt RJ. *Concepts and Applications of Finite Element Analysis*. Hoboken, NJ: John Wiley & Sons; 2007.

APPENDIX A

PLANE STRAIN NONLINEAR ELASTIC CONSTITUTIVE MODEL

Consider the strain tensor $\boldsymbol{\varepsilon}$ for plane strain problems. The matrix representative of $\boldsymbol{\varepsilon}$ is given by

$$[\boldsymbol{\varepsilon}] = \begin{bmatrix} \varepsilon_{11} & \varepsilon_{12} & 0 \\ \varepsilon_{12} & \varepsilon_{22} & 0 \\ 0 & 0 & 0 \end{bmatrix}. \tag{A1}$$

The deviatoric strain tensor $\boldsymbol{\varepsilon}_d$ is defined as

$$\boldsymbol{\varepsilon}_d \equiv \boldsymbol{\varepsilon} - \frac{1}{3}(\text{tr}\boldsymbol{\varepsilon})\boldsymbol{I} \tag{A2}$$

with norm

$$\|\boldsymbol{\varepsilon}_d\| = \sqrt{\boldsymbol{\varepsilon}_d : \boldsymbol{\varepsilon}_d}. \tag{A3}$$

The nonlinear elastic constitutive relationship can be written in the following form:

$$\boldsymbol{\sigma} = K\varepsilon_v\boldsymbol{I} + 2\mu(\|\boldsymbol{\varepsilon}_d\|)\boldsymbol{\varepsilon}_d, \tag{A4}$$

where the expression for $\mu(\|\boldsymbol{\varepsilon}_d\|)$ in (A4) is

$$\mu(\|\boldsymbol{\varepsilon}_d\|) = \frac{\sqrt{2}\tau_y}{2}\frac{1}{\varepsilon_{\text{ref}} + \|\boldsymbol{\varepsilon}_d\|}, \tag{A5}$$

in which ε_{ref} is a small reference strain.

The consistent tangent matrix $\boldsymbol{D}$ is

$$\boldsymbol{D} = \frac{\partial\boldsymbol{\sigma}}{\partial\boldsymbol{\varepsilon}} = \boldsymbol{D}_v + \boldsymbol{D}_{d1} + \boldsymbol{D}_{d2}, \tag{A6}$$

where

$$\boldsymbol{D}_v = K\begin{bmatrix} 1 & 1 & 0 \\ 1 & 1 & 0 \\ 0 & 0 & 0 \end{bmatrix}, \quad \boldsymbol{D}_{d1} = \mu(\|\boldsymbol{\varepsilon}_d\|)\begin{bmatrix} \frac{4}{3} & -\frac{2}{3} & 0 \\ -\frac{2}{3} & \frac{4}{3} & 0 \\ 0 & 0 & 1 \end{bmatrix}, \tag{A7}$$

and

$$\boldsymbol{D}_{d2} = \frac{2}{\|\boldsymbol{\varepsilon}_d\|}\frac{d\mu(\|\boldsymbol{\varepsilon}_d\|)}{\|\boldsymbol{\varepsilon}_d\|}\bar{\boldsymbol{\varepsilon}}\,\bar{\boldsymbol{\varepsilon}}^{\text{T}}, \tag{A7}$$

with $\bar{\boldsymbol{\varepsilon}}^{\text{T}} = \left[\varepsilon_{11} - \frac{1}{3}(\varepsilon_{11} + \varepsilon_{22}), \ \varepsilon_{22} - \frac{1}{3}(\varepsilon_{11} + \varepsilon_{22}), \ \varepsilon_{12}\right]$. At the origin, ie, $\varepsilon_{11} = \varepsilon_{22} = \varepsilon_{12} = 0$, the consistent tangent matrix $\boldsymbol{D}_0$ becomes

$$\boldsymbol{D}_0 = \boldsymbol{D}_v + \boldsymbol{D}_{d1}. \tag{A8}$$

For $\varepsilon_{\text{ref}} = \tau_y \sqrt{2 \frac{(1+v)}{E}}$, the consistent tangent matrix can be conveniently written as

$$\boldsymbol{D}_0 = \frac{E}{(1-2v)(1+v)} \begin{bmatrix} 1-v & v & 0 \\ v & 1-v & 0 \\ 0 & 0 & \frac{(1-2v)}{2} \end{bmatrix},$$ (A9)

which, as expected, is the same as the linear elastic case.[35]

APPENDIX B

LOWER-BOUND THEOREM

Chen and Han[14] stated the lower-bound theorem as follows:

"*If an equilibrium distribution of stress σ_{ij}^E can be found which balances the body force F_i in V and the applied loads T_i on the stress boundary A_T and is everywhere below yield, $f(\sigma_{ij}^E) < 0$, then the body at the loads T_i, F_i will not collapse.*"

In the analysis of the optimized clamped beam topologies considering the nonlinear elastic model, every stress state is below the von Mises yielding limit, as shown in Figure 16B. Therefore, on the basis of the lower-bound theorem, we conclude that the asymptotic nonlinear elastic analysis leads to a more conservative (ie, safer) design.

APPENDIX C

FAILURE MECHANISM OF THE OPTIMIZED CLAMPED BEAM STRUCTURE

As part of the verification of the optimized clamped beam structures in Section 6.3, we investigated the failure mechanism of the optimized structures under limit pressures considering classical Mises plasticity. Figure C1 shows the contours of equivalent plastic strain (PEEQ) for the three optimized beam structures. In each of the three contours, development of plastic yielding is observed near the supports. In Figure C1.A, plastic yielding in Zone 1 develops more obviously than that in Zone 2. However, the development of plastic yielding in Zones 1 and 2 is similar in Figure C1.B and C1.C. Qualitatively, the optimized clamped beam structure with a higher limit pressure tends to have similar development of plastic yielding at supports. This observation can inform engineering intuition on optimal plastic material designs.
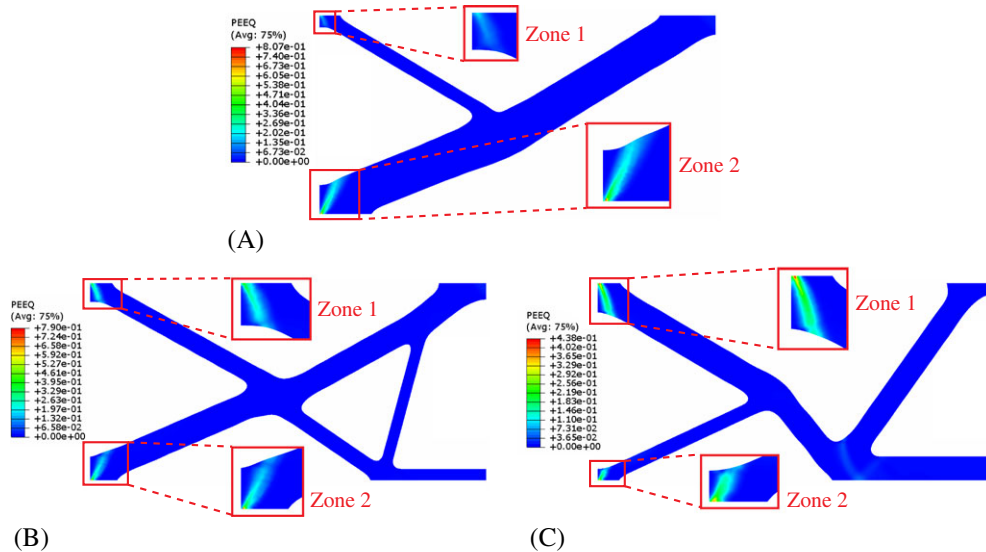

FIGURE C1 Contour plots of equivalent plastic strain for (A) topology I under its limit pressure $w = 101.325$ kPa, (B) topology II under its limit pressure $w = 134.993$ kPa, and (C) topology III under its limit pressure $w = 137.801$ kPa

APPENDIX D

A CONTINUATION SCHEME OF FILTER ORDER (q)

For removing the unnatural slender members in the optimized structures, we use a filter-order continuation scheme so that the quality of the nonlinear result can be improved. The filter-order continuation scheme is based on the density filter. The relationship between filtered densities $\overline{\rho}$ and density variables ρ can be written as[33]

$$\overline{\rho} = \mathbf{H}\rho, \tag{D1}$$

where $\mathbf{H}$ is the filter matrix, which is defined as

$$H_{ij} = \frac{h(i,j)v_j}{\sum_k^n h(i,k) v_k}, \qquad h(i,j) = \max\left\{ 0, \quad [r_{\min} - \text{dist}(ij)]^q \right\}, \tag{D2}$$

where v_e is the volume of the eth element, n is the number of elements in the discretization, $r_{\min}$ is the filter radius, dist(i,j) is the operator defining the distance $\overline{\rho}$ and ρ, and the exponent q is the order of the filter.

The idea of the continuation scheme is to start the optimization iteration with a linear ($q = 1$) filter and then apply a higher-order ($q = 2$ or 3) filter after the solution converges. For example, Figure D1 illustrates the convergence history of the 1 m × 1 m, three fixed-sides beam problem solved in Section 6.4. A linear filter ($q = 1$) is used starting from iteration #1 until the solution converges at iteration #423. At the next iteration #424, we use a quadratic ($q = 2$) filter only for this single optimization step. From iteration #425 to iteration #824, the linear filter ($q = 1$) is used again until convergence of the solution. At iteration #825, we repeat the strategy described above. Comparing the topologies at iterations #423, #824, and #1150, we verify that the slender members on the top portion of the structure are removed. In addition, the objective (U) is slightly improved, as shown in Table D1.
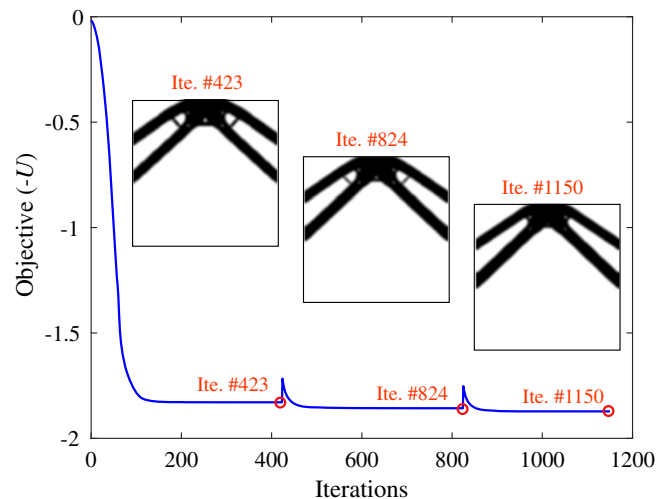

FIGURE D1   Convergence history for the 1 m × 1 m beam of Figure 17B, illustrating the filter-order continuation scheme [Colour figure can be viewed at wileyonlinelibrary.com]

TABLE D1   Comparison of the objective (U) obtained with the filter-order continuation scheme

	Ite. #423, MJ	Ite. #824, MJ	Ite. #1150, MJ
Objective (U)	1.8289	1.8570	1.8721

APPENDIX E

THE CHOICE OF THE PRESCRIBED ENERGY C_0

For illustrative purposes, let us consider the particular case of linear elasticity, in which Equation (20) can be written as

$$\begin{cases} \boldsymbol{K}\,\boldsymbol{u} = \lambda\boldsymbol{f}_0 \\ \boldsymbol{f}_0^{\mathrm{T}}\,\boldsymbol{u} = 2C_0, \end{cases} \tag{E1}$$

where $\boldsymbol{K}$ is the stiffness matrix, $\boldsymbol{u}$ is the displacement vector, $\boldsymbol{f}_0$ is the external force vector, and λ is the Lagrange multiplier, which is also the load factor associated with the reaction forces. We verify that Equation (E1) is mathematically equivalent to the state equation proposed by Klarbring and Strömberg[20] as

$$\begin{cases} \boldsymbol{K}\,\boldsymbol{u} = \boldsymbol{f}_0 + \bar{\lambda}\,\boldsymbol{e} \\ \boldsymbol{e}^T\,\boldsymbol{u} = \delta, \end{cases} \tag{E2}$$

where $\boldsymbol{e}$ is a prescribed column vector and δ is a prescribed displacement. In Klarbring and Strömberg's state equation (E2), the displacement δ is prescribed as the kinematic constraint, and the Lagrange multiplier $\bar{\lambda}$ has the unit of force. By comparison, we prescribe the energy C_0 in our approach, and thus, the Lagrange multiplier λ in Equation (E1) is adimensional.

In the following, we use a simple three-bar truss example to (i) explain how to estimate a value for C_0 and (ii) demonstrate how to solve the structural problem with the state equation (E1).

The three bars, as shown in Figure E1, have the same circular cross section with diameter $d = 0.005$ m, and they are made of a linear elastic material with Young's modulus $E = 10^8$ kPa. Two external forces are applied at node 2 (vertical) and at node 3 (horizontal), respectively. The magnitude of the external load P is 10 kN.

Let us assume that the designer suggests to prescribe a vertical displacement $u_{2y} = -0.012$ m at node 2 and a horizontal displacement $u_{3x} = 0.015$ m at node 3, respectively. On the basis of the designer's request, we can estimate C_0 as

$$C_0 = \frac{1}{2}\,\left(-Pu_{2y} + 1.5Pu_{3x}\right) = 0.1725 \text{ kN} \cdot \text{m}. \tag{E3}$$

To solve this structural problem, the state equations (E1) can be written in matrix form as

$$\begin{bmatrix} \boldsymbol{K} & -\boldsymbol{f}_0 \\ -\boldsymbol{f}_0^{\mathrm{T}} & 0 \end{bmatrix} \begin{Bmatrix} \boldsymbol{u} \\ \lambda \end{Bmatrix} = \begin{Bmatrix} \boldsymbol{0} \\ -2C_0 \end{Bmatrix}. \tag{E4}$$

From Equation (E4), $\boldsymbol{u}$ and λ can be solved numerically as

$$\begin{Bmatrix} \boldsymbol{u} \\ \lambda \end{Bmatrix} = \begin{bmatrix} 522.59 & -4.14 & -175.58 & 0 \\ -4.14 & 1049.32 & 351.15 & 10 \\ -175.58 & 351.15 & 829.91 & -15 \\ 0 & 10 & -15 & 0 \end{bmatrix}^{-1} \begin{Bmatrix} 0 \\ 0 \\ 0 \\ -0.345 \end{Bmatrix} = \begin{Bmatrix} 0.0052 \\ -0.0107 \\ 0.0159 \\ 0.5665 \end{Bmatrix}. \tag{E5}$$
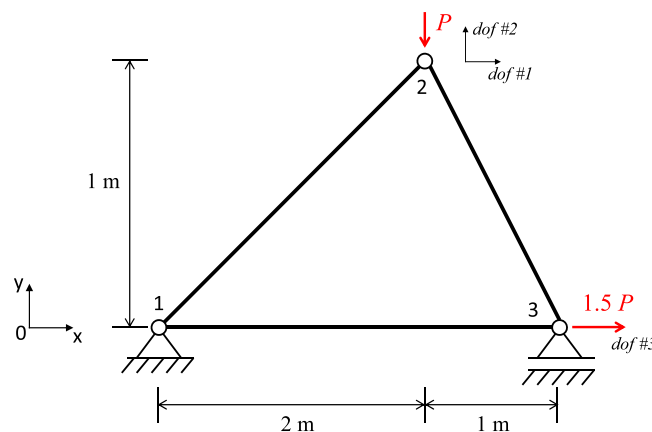

FIGURE E1 The three-bar truss example [Colour figure can be viewed at wileyonlinelibrary.com]

Therefore, we obtain $\boldsymbol{u}$ and λ as

$$\boldsymbol{u} = \begin{bmatrix} 0.0052 & -0.0107 & 0.0159 \end{bmatrix}^{\mathrm{T}} \mathrm{m} \qquad \lambda = 0.5665. \tag{E6}$$

From the Equation (E6), we can verify that $C_0 = 1/2(-Pu_{2y} + 1.5Pu_{3x}) = 0.1725\,\mathrm{kN \cdot m}$, which is identical to the energy we estimated in Equation (E3).

APPENDIX F

ONE-BAR TRUSS EXAMPLE

We use a simple one-bar truss example to (i) illustrate that both formulations (ie, max U and max λ) lead to optimal designs in terms of stiffness and (ii) demonstrate the relationship between the strain energy (U) and the prescribed energy (C_0). The one-bar truss structure, as shown in Figure F1, is fixed at the left end, and it is made of linear elastic material with Young's modulus E. The length and the cross-sectional area of the truss are L and A, respectively. An external force f_0 is applied at the right end, and the displacement of this end is u.

For this one-dimensional case, the state equation (20) in the linear elastic case becomes

$$\begin{cases} K\,u = \lambda\,f_0 \\ f_0\,u = 2C_0, \end{cases} \tag{F1}$$

where $K = AE/L$ is the stiffness of the truss. By solving Equation (F1), we can obtain λ as

$$\lambda = 2\left(\frac{AE}{L}\right)\frac{C_0}{f_0^2}. \tag{F2}$$

Equation (F2) shows that maximizing the load factor λ is equivalent to maximizing the stiffness of the truss structure. In addition, the strain energy of the truss can be written as

$$U = \frac{1}{2}\left(\frac{AE}{L}\right)u^2 = \frac{1}{2}\left(\frac{AE}{L}\right)\left(\frac{2C_0}{f_0}\right)^2 = 2\left(\frac{AE}{L}\right)\frac{C_0^2}{f_0^2}. \tag{F3}$$

Similarly, from Equation (F3), we find that maximizing the strain energy U is equivalent to maximizing the stiffness of the truss. By comparing Equations (F2) and (F3), we obtain that

$$C_0 = \frac{U}{\lambda}. \tag{F4}$$

Therefore, Equation (F4) demonstrates the linear relationship between the prescribed energy C_0 and the strain energy U considering the linear elastic case. This conclusion is verified numerically by the three-support beam example in Section 6.1. In this example, the equality $C_0 = U/\lambda$ holds when we consider $C_0 = 10^{-4}$ kJ, which represents the linear elastic case (see Table 8).

FIGURE F1 The one-bar truss example [Colour figure can be viewed at wileyonlinelibrary.com]